

Self-organised vegetative patterns: The pathway to ecosystem collapse

Charles Cameron

September 2022

MTHM021

MSc Mathematical Modelling (Biology and Medicine)

Abstract

Striking vegetative patterns are seen in semi-arid environments. The pattern are self-organised via short range cooperation between plants and long-range competition over resources. This project will analyse and simulate the Klausmeier model (Klausmeier 1999) a partial differential model explaining the relationship between water flow and spatial dispersal of plants. On sloped terrain vegetative bands form and slowly migrate uphill forming a stable travelling wave. The interaction of the spatially diffusing vegetation and downhill flowing water results in the formation of spatial bands. The patterns form from diffusion-driven instability, a concept introduced by Alan Turing (Turing 1952). The patterns in vegetation form when the system is critically close to becoming a desert, with increasing band periods paving the way to an eventual ecosystem collapse. The vegetative patterns exist in extremely hostile conditions and signify the resilience of the formation.

Acknowledgements

I would like to thank my supervisor Professor Sieber for all the guidance he gave throughout the Masters project. To Professor Biktashev who offered pointers in the project presentation.

Contents

1 Literature review	4
1.0.1 Vegetative patterns: Structure and causes	4
1.0.2 Theoretical models to explain the phenomenon	6
1.0.3 Turing instability: The mechanism behind the patterns	8
1.0.4 Extended partial differential model	8
1.0.5 Critical transitions and the significance of spatial organisation	9
2 Klausmeier model analysis	11
2.1 Locating the uniformly stable steady states	12
2.2 Stability analysis of spatially uniform equilibria with non-uniform perturbations	15
2.2.1 Boundary conditions	17
2.2.2 The Desert steady state	17
2.2.3 Vegetative steady state	18
3 PDE simulation	21
3.1 Finite-difference approximation	21
3.2 Stability of different numerical methods	22
3.2.1 Explicit Euler method	22
3.2.2 Implicit Euler method	23
3.2.3 The Crank-Nicolson method	23
3.3 Discretisation of the differential operator	24
3.4 Numerical accuracy	27
4 PDE simulation observations	29
4.1 Initialising the simulation	29
4.2 Random initial conditions	30
4.3 Frequency analysis	31
4.3.1 Final frequency	34
4.3.2 Bottleneck frequency	35
4.4 Wave speed analysis	36
4.5 Frequency growth rate	37
4.6 The wavelength of the solution	38
4.7 Conclusions	39
5 Existence of travelling waves	40
5.1 Bifurcation analysis of the travelling wave solutions	41
5.1.1 Fixing the period	42
5.2 Critical transitions	43
5.3 Conclusion	46
A Appendix Title	47
A.1 Functions	47
A.1.1 Locating equilibria	47
A.1.2 Eigenvalues	47
A.1.3 Terms of the Crank-Nicolson method	48
A.1.4 The Crank-Nicolson method	48

CONTENTS

A.2 Main code	49
-------------------------	----

Chapter 1

Literature review

1.0.1 Vegetative patterns: Structure and causes

It has long been observed in the field of plant ecology that vegetation is often arranged over large areas in a non-uniform and a non-random arrangement (Greig 1979; Lefever and Lejeune 1997). Striking self-organised vegetative patterns are seen in semi-arid areas of America, Africa, Asia, and Australia (Rietkerk, Boerlijst, et al. 2002). Semi-arid areas cover a large proportion of the earths continental surface and characterised by desert-like condition, extended dry periods and low water availability inhibiting plant growth (Rietkerk, Boerlijst, et al. 2002; Lejeune, Couteron, and René Lefever 1999).

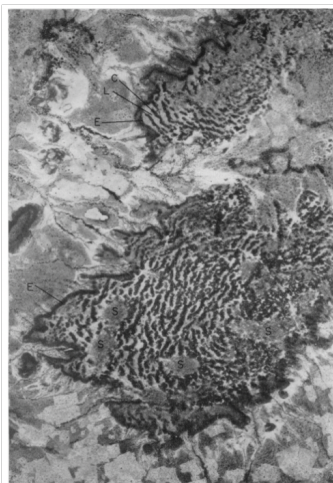


Figure 1.1: Figure taken from White 1970: 1 : 25000 scale air photograph of brousse tigrée on dissected plateau blocks at $13^{\circ}6'N, 4^{\circ}4'E$ in the 700 mm rainfall zone. C, Linear woodland; L, open lane; E, escarpment of the laterite cuirass; S, small dumps of wind-blown sand.

The modern-day understanding is that these patterns are different manifestations of the same ecological phenomena Lejeune, Couteron, and René Lefever 1999 in which scale-dependent feedback over limited resources results in self-organised patterns. The pattern is intrinsically generated (Rietkerk, Boerlijst, et al. 2002). Plants group together forming bare patches rather than uniformly decreasing in density. Figure 1.1 and 1.2 show striped and spotted patterns formed in Niger.

The vegetative patterns are characterised by the spatial regularity and the vast area it covers (Lejeune, Couteron, and René Lefever 1999). The first observation of this phenomena dates to the mid 20th century (MacFayden 1950) in which ‘rhythmic patterns of the vegetation’ were observed from aerial photographs over the then British Somaliland. The paper remarks that aerial photographs are crucial as such patterns would be impossible to recognise in the field.

The striped vegetative pattern has since been named *Tiger Bush* or *Brousse tigrée* as often seen in

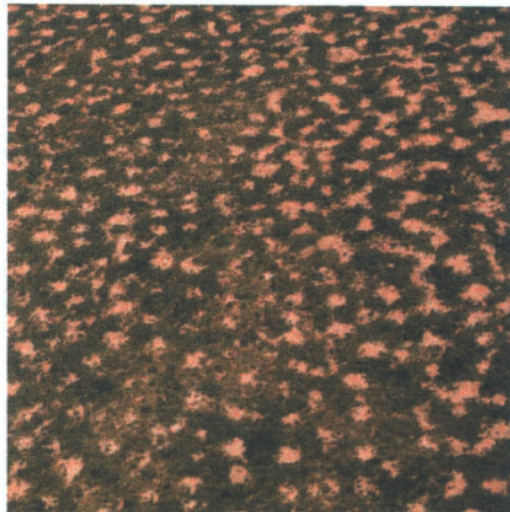


Figure 1.2: Figure taken from (Rietkerk, Boerlijst, et al. 2002): *Aerial photographs from patterned vegetation in Niger (S.Prince, personal communication)*. Scale is 400×400 Labyrinths with spots.

the french speaking Niger (White 1970). The aerial photograph, Figure 1.1, features Combretum woodland on a semi-arid plateau located in Niger. The woodland has more or less equal width vegetation bands of 35-40 metres in width. White made comparisons between the yearly annual recorded rainfall and the types of patterns seen with results suggesting that in lower rainfall areas the bands are spread further apart and for rainfall levels greater than 750mm then uniform vegetative coverage is seen. The bands were observed to lie orthogonal to the gradient of the slope and act to ‘dam’ the water run-off. The paper states that the ultimate pattern is determined by the level of rainfall and reinforced by herbivores grazing on the band’s margins. The bare areas were suggested to be formed from initial termite activity and remain uncolonised by the ‘self-perpetuating’ patterns. The following year White suggested that patterns could also be attributed to the decline of soil fertility and climactic changes.

The vegetative bands are arranged in bands by means of survival; a community of plants will be better protected against the hostile conditions. Field data supports that plants have a positive impact on one another in harsh conditions and that a dominating species would influence the location of other flora (Greig 1979). This positive influence of larger shrubs in semi-arid is referred to as ‘Islands of fertility’ (Schlesinger et al. 1996). Numerous other studies demonstrate facilitative interaction of plants (Callaway 1995) and that plants increase the rate that water infiltrates the soil which later becomes an integral concept to the mathematical models.

A 1999 study (Valentin, d’Herbes, and Poesen 1999) collected observations and results over many decades to understand the relationship between environmental factors and the types of vegetative patterns that develop. The researchers stated the difficulty linking data as patterns were interpreted, categorised, and named differently for each study. Crucially for vegetative patterns to form then its critical that ‘overland flow cannot concentrate’. The study linked the vegetative patterns to the level of rainfall and the slope of the environment, presented in Figure 1.3. The contrast between bare soil and plants decreases with increasing rainfall forming a ‘fuzzy pattern’. As the level of rainfall reduces there is a greater contrast forming a ‘dashed pattern’ of longer spatial periods but reduced band length. Spotted patterns emerge in flat regions.

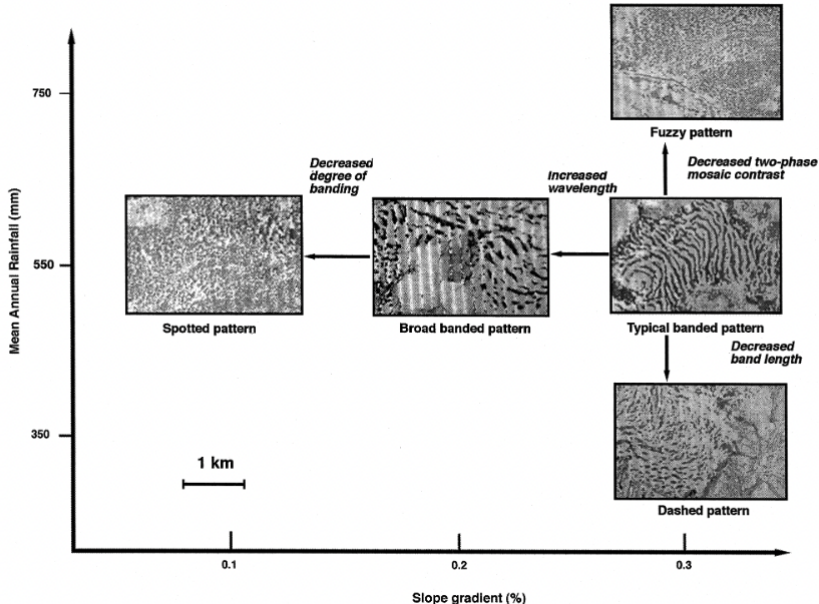


Figure 1.3: Figure taken from (Valentin, d'Herbes, and Poesen 1999): *Typical type of banding vegetation patterns and possible variants examples from Niger.*

The Tiger bush arrangement had been recorded in qualitative terms from (White 1970), (Greig 1979) and later (Thiery, D'Herbes, and C. Valentin 1995). The latter paper formalised the water redistribution hypothesis on a slope and that the ‘pioneering’ front of the vegetative band will collect more water and migrate uphill. Field evidence does support the migration hypothesis (Valentin, d'Herbes, and Poesen 1999) however notable movement takes decades to observe, often both costly and tedious.

1.0.2 Theoretical models to explain the phenomenon

The first formalised theory to suggest that the patterns had an intrinsic mechanism was put forward in the 1997 paper *On the origin of Tiger bush* (Lefever and Lejeune 1997). The paper introduced that vegetative patterns would form from ‘symmetry breaking instability’ governed by the combination of short-range positive feedback controlling plant reproduction and the long-range negative feedback caused by the overall competition over resources. The authors Lefever and Lejeune suggested a possible mechanism to model plant density $c(x, t)$ (Plant biomass per unit area) over time.

$$\frac{\partial c}{\partial t} = \underbrace{F_1 \times F_2}_{\text{Growth term}} - \underbrace{F_3}_{\text{Death term}} \quad (1.1)$$

The functions are non-negative and describe particular biological processes. The function F_1 models the reproduction of plants, F_2 the interaction between plants and prevents the density increasing beyond biologically feasible. The term F_3 accounts for the natural death rate. The rate of reproduction is favourably influenced by a high vegetative density; this is given by a non-linear quadratic function. At further distances plants no longer cooperate and inhibit mutual growth (Due to competition). The model has a variable death rate depending on the proximity of nearby plants. This model is highly complex and includes many variable functions depending on particular quantities. The model simulates vegetative stripes similar to Tiger bush and more dashed and spotted pattern.

The Klausmeier model is an influential and well-established mathematical model which explains the *Tiger bush* phenomenon both in formation and subsequent uphill propagation of the bands (Klausmeier 1999). A pair of partial differential equations for the level of surface water ($w(x, t)$)

and plant biomass ($u(x, t)$), assuming the downhill flow of water on a steady slope. The unit of time used in years, and spatial units metres (before nondimensionalisation)

This model assumes that plant growth directly depends on the amount of available infiltrated water which is accelerated by a high plant density. The nondimensionalised model has clear biological parameters concerning the rate of evaporation, rainfall levels and slope gradient. This model is a bistable system (Rietkerk, Dekker, et al. 2004); two stable states of attraction (Desert and non-desert). The nondimensionalised partial differential model is

$$\begin{aligned} \frac{\partial u}{\partial t} &= \underbrace{wu^2}_{\text{Plant growth}} - \underbrace{bu}_{\text{Plant loss}} + \underbrace{\left(\frac{\partial^2 u}{\partial x^2} + \frac{\partial^2 u}{\partial y^2} \right)}_{\text{Plant dispersal}} \\ \frac{\partial w}{\partial t} &= \underbrace{a}_{\text{Rainfall}} - \underbrace{w}_{\text{Evaporation}} - \underbrace{wu^2}_{\text{Uptake by plants}} + \underbrace{\nu \frac{\partial w}{\partial x}}_{\text{Downhill flow}} \end{aligned} \quad (1.2)$$

The non-linear term wu^2 forms a positive feedback cycle. The rate that plants grow depends on the density and results from the facilitate dynamics between plants and soil infiltration. The numerical simulations Klausmeier 1999 determined that striped patterns developed from non-uniform spatial perturbations to the stable vegetative steady state, below some critical threshold for a . With decreasing rainfall the period of the stripes increase before eventually transitioning to the desert state. The numerical simulations form patterns from initial perturbations in a process similar to Turing-instability (Turing 1952) as in this case there is an advection term alongside diffusion. Klausmeier chose plausible parameters based on field results. The evaporation rates were assumed from (Mauchamp, Rambal, and Lepart 1994) and vegetative pattern observation seen in (Worral 2006, Originally published 1959) and (White 1970). The bands of grass are estimated to move from $0.3 - 1.5\text{m}/\text{yr}$ (Worral 2006).

Klausmeier acknowledged the equations were a great simplification, for example, not separating the surface and soil water. This model can be considered in one or two dimensional space.

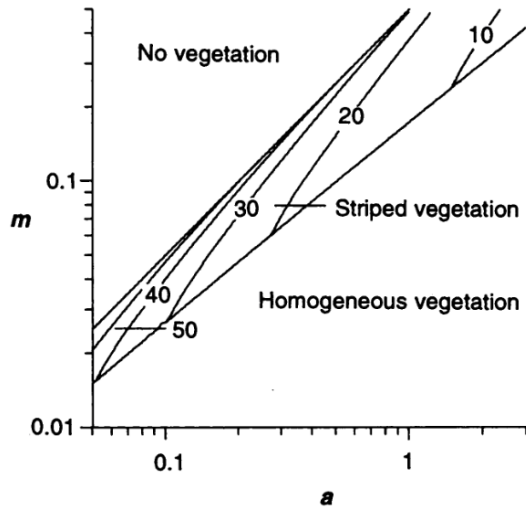


Figure 1.4: Figure taken from (Klausmeier 1999)), Note parameters names have been adjusted. The parameter m , the death rate, is taken to be b in this analysis : *Behavior of the model as determined by the water input rate a and plant loss rate b when water velocity $\nu = 182.5$. The contours give the dimensional stripe wavelength in meters as determined by the most unstable mode found with linear stability analysis. As water input is decreased or plant loss is increased, the model predicts a transition from homogeneous vegetation, to stripes of increasing wavelength, to no vegetation*

1.0.3 Turing instability: The mechanism behind the patterns

The Klausmeier model demonstrated that spatial patterns form from Diffusion-driven instability, a biological phenomenon introduced nearly 50 years previously by the acclaimed mathematician Alan Turing (Turing 1952). The seminal idea put forward by Turing was that the self-organised embryonic tissue differentiation was in response to underlying spatial heterogeneity's in the concentration of chemical 'morphogens'. In a developing system either chemical will have a uniformly stable steady state however this can be driven unstable through the process of diffusion, a novel idea as diffusion was long considered a stabilising process; the interaction of different stabilising processes could in fact result in instability (Maini et al. 2012). In the absence of diffusion the steady states would be stable. Turing analysis on unstable growing modes was a relatively new concept for this field at the time, (Lefever and Lejeune 1997). Turing studied the following model (Maini et al. 2012):

$$\frac{\partial \mathbf{u}}{\partial t} = \mathbf{f}(\mathbf{u}) + \mathbf{D}\nabla^2\mathbf{u} \quad (1.3)$$

This models a pair of interacting chemical concentration $\mathbf{u} = (u, v)^t$. The reaction-kinetics of the chemical species are modelled by the, generally non-linear, reaction term $\mathbf{f}(\mathbf{u})$. Either chemical diffuses over space at some rate given by the diagonal entry in the matrix \mathbf{D} . The *diffusion-driven-instability* will cause wave-like patterns to form of particular frequencies. The Klausmeier model is similar to the reaction-diffusion equation except the water flows downhill rather than diffuses outwards resulting travelling patterns (J.A Sherratt 2013; Klausmeier 1999)

1.0.4 Extended partial differential model

The spatially explicit partial differential model put forward (Rietkerk, Boerlijst, et al. 2002) aims to explains the mechanism behind different pattern formation. This builds on the previous non-spatial differential model (Koppel, Rietkerk, and Weissing 1997) and (Klausmeier 1999). This model aims to fill in the theoretical gaps of the Klausmeier model describing both surface and soil water (mm) separately. The model assumes that water diffuses over space rather with a net displacement of water from bare soil to areas of higher vegetative density measured (gm^{-2}). This model was later extended to include sloped terrain by replacing the surface water flow diffusion term with an advection term (Rietkerk, Dekker, et al. 2004).

This is a complex and comprehensive model including the maximum soil infiltration rate, the rate that plants uptake water and the reduced infiltration rate in the absence of plants. Unlike the Klausmeier model numerical simulation form patterns on flat surfaces which describing the moasic and spotted styles seen. The numerical models are a great simplification of reality ignoring the influences of grazing, soil erosion, non-uniform terrain and variances in soil fertility (Rietkerk, Boerlijst, et al. 2002). The model uses three variables: Plant density ($P; gm^{-2}$), Soil water ($W; mm$) and finally surface water ($O; mm$).

$$\begin{aligned} \frac{\partial P}{\partial t} &= \overbrace{c \times g_{max} \times \frac{W}{W + k_1} \times P - d \times P + D_p \nabla^2 P}^{\dagger_1} \\ \frac{\partial W}{\partial t} &= \overbrace{\alpha \times O \frac{P + k_2 \times W_0}{P + k_2} - g_{max} \times \frac{W}{W + k_1} \times P - r_w \times W + D_w \nabla^2 W}^{\dagger_2} \\ \frac{\partial O}{\partial t} &= R - \underbrace{\alpha \times O \frac{P + k_2 \times W_0}{P + k_2} + D_O \nabla^2 O}_{\dagger_2} \end{aligned} \quad (1.4)$$

The core components of the model will be analysed, the reader must refer to the original material (Rietkerk, Boerlijst, et al. 2002) for a comprehensive understanding of the model parameters. Firstly each partial differential contains a Laplacian operator ∇^2 which models the relevant diffusion over space of rate D . The rate of diffusion is highest for surface water as expected. The component labelled \dagger_1 demonstrates that the rate of vegetative growth is proportional to the level

of soil water, which is limited by the k_1 component which controls the rate of water uptake. The component labelled \dagger_2 is integral to the mechanism, demonstrating that the level of infiltrated water directly depends on the density of vegetation (introducing the plant facilitation component). The level of surface water depends on the fixed rate of rainfall R with \dagger_3 the opposite of \dagger_2 (Which accounts for the relative loss of surface water due to infiltration). The Laplacian operator for the surface water level can be switched to an advection term (∇O) for sloped terrain.

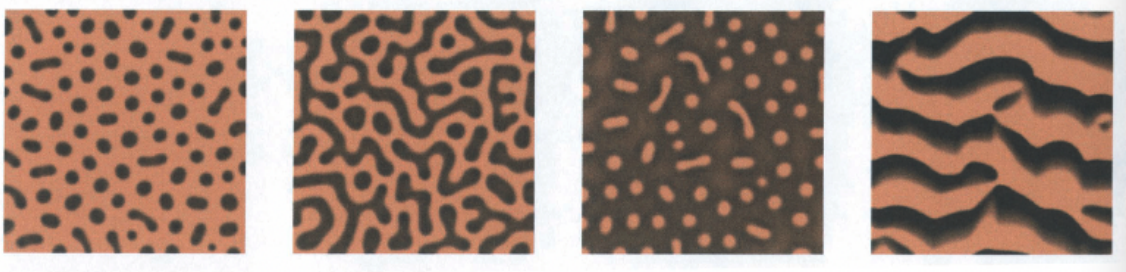


Figure 1.5: Figure taken from (Rietkerk, Boerlijst, et al. 2002)), Note *a, b, c, d* reads right to left: *Spatial patterns for different amounts of rainfall (R) after t = 3,000d. Scale is 400 × 400 Plant mortality, d, is 0.25, with other parameters set as default values (see text). Plants are represented by dark green and bare soil by light brown. An animation of this model output is available on the online edition of The American Naturalist as an appendix. a, Spotted pattern, R = 0.75; b, labyrinths with spots, R = 1.0; c, gap pattern, R = 1.25; d, regular bands on slope (top on right 1.0R periodic boundary conditions), R = 1.*

The numerical simulations of the model, Figure 1.5 shows that as rainfall increases then the arid areas become sparse. There seems to be almost a switch of spots of vegetation to spots of bare soil, which supports the (Valentin, d'Herbes, and Poesen 1999) generalised diagram (see Figure 1.3). The simulation results on sloped terrain strongly agree with the Klausmeier model (Rietkerk, Boerlijst, et al. 2002).

1.0.5 Critical transitions and the significance of spatial organisation

All Ecosystems are constantly exposed to gradual changing conditions from the level of rainfall through to the loss of species. It is expected that the natural system will smoothly respond to the change to minimise the impact. Ecological studies show that a system may suddenly switch to a contrasting state (Scheffer et al. 2001a). This sudden shift marks a catastrophic change in both the organisation and functioning of an ecosystem (Scheffer et al. 2001b). Often seen in multi-species systems which possess multiple different stable equilibrium points. Large disturbances will force the system to converge to the alternate state described as a ‘ball in a pin-ball machine’ (May 1977) causing the extinction of a species. A more resilient system will be able to endure large perturbations without the system collapsing to the alternative state (Holling 1973).

The partial differential models for vegetative density have two spatially uniform steady states (Desert and non-desert). The dynamics of either model is determined by the attraction to either steady state with a critical transition marking the switch to the desert. As the environmental conditions approach this critical transition spatial patterns emerge ‘bridging the gap’ (Rietkerk, Dekker, et al. 2004) between either environmental state.

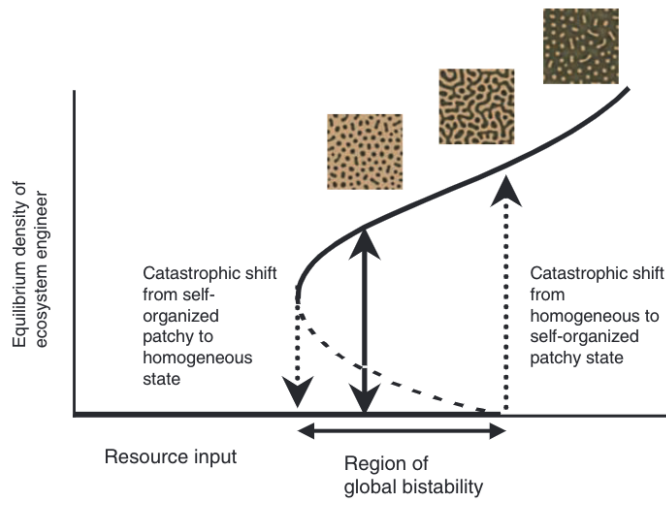


Figure 1.6: Figure taken from (Rietkerk, Dekker, et al. 2004)): *Model showing how ecosystems may undergo a predictable sequence of emerging self-organized patchiness as resource input decreases or increases. Thick solid lines represent mean equilibrium densities of consumers functioning as ecosystem engineers. Dotted arrows represent catastrophic shifts between self-organized patchy and homogeneous states, and vice versa. Dark colors in the insets represent high density. The range of resource input for which global bistability and hysteresis exists is between these dotted arrows. Solid arrows represent development of the system toward the coexisting self-organized patchy state or homogeneous state, depending on initial ecosystem engineer densities*

Numerical simulations demonstrate that self-organised patchiness exists within the parameter range of system bistability, Figure 1.6. The upper limit has been since named as the Turing-Hopf (super-critical) bifurcation point (Stelt et al. 2013). Patterns had long been considered a sign of system collapse however its now accepted that the self-organisation is more a sign of resilience (Rietkerk, Bastiaansen, Banerjee, Jvan de Koppel, et al. 2021). Further study on the generalised Klausmeier model (Stelt et al. 2013) demonstrated that vegetative patterns will exist beyond this tipping point in the parameter region called the *Busse Balloon*. Rietkerk amended the analysis (Rietkerk, Bastiaansen, Banerjee, Jvan de Koppel, et al. 2021) illustrating that spatial self-organisation persists beyond the tipping point forming a 'pathway evading tipping' for lower levels of rainfall.

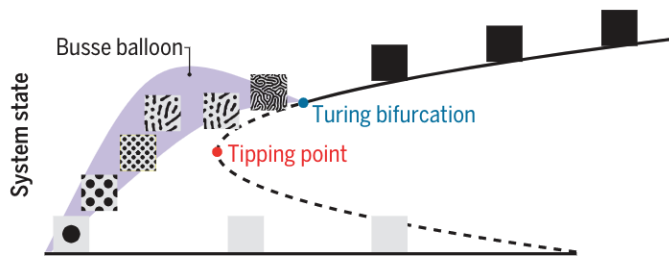


Figure 1.7: Figure taken from (Rietkerk, Bastiaansen, Banerjee, Jvan de Koppel, et al. 2021)): *Multistability of Turing patterns. Here, spatial self-organization through Turing instability arises in parameter regions before the tipping point at the Turing bifurcation, persisting beyond the tipping point, thereby constituting a pathway evading tipping through spatial pattern formation.*

The *Busse balloon* forms at the Hopf-Turing bifurcation point and 'persists beyond the tipping point'. The limits of the balloon define the upper and lower margins of plant density for that particular level of rainfall.

Chapter 2

Klausmeier model analysis

The model, designed by Christopher Klausmeier (Klausmeier 1999), explains the formation and subsequent migration of vegetative bands on sloped terrain in semi-arid environments. The general mechanism is that water runs downhill over bare soil and absorbed by the *pioneering* front of the vegetative band (Thiery, D'Herbes, and C. Valentin 1995), causing the entire band to migrate uphill. This project will only consider the vegetative density along the X -axis which is the direction that the water flows. The complete model is given by the following (Klausmeier 1999):

$$\begin{aligned}\frac{\partial U}{\partial T} &= RJWU^2 - MU + D \left(\frac{\partial^2}{\partial X^2} + \frac{\partial^2}{\partial Y^2} \right) U \\ \frac{\partial W}{\partial T} &= A - LW - RWU^2 + V \frac{\partial W}{\partial X}\end{aligned}\tag{2.1}$$

The pair of partial differential model the plant biomass (U) and the level of surface water (W). The model assumes constant rainfall (A) and evaporation proportional to (LW). The function RWU^2 is the non-linear term that accounts for plants increasing the rate that water infiltrates the soil. The slope of the gradient (and rate that water flows downhill) is given by the term V . The variable J is the yield of plant biomass per unit water consumed and D the diffusion constant.

The paper(Klausmeier 1999) nondimensionalised the equation 2.1, making the substitutions: $w = R^{\frac{1}{2}}L^{-\frac{1}{2}}JW, u = R^{\frac{1}{2}}L^{-\frac{1}{2}}U, x = L^{\frac{1}{2}}, t = LT, a = AR^{\frac{1}{2}}L^{-\frac{3}{2}}J, \nu = VL^{-\frac{1}{2}}D^{-\frac{1}{2}}$.

$$\begin{aligned}\frac{\partial u}{\partial t} &= \underbrace{wu^2}_{\text{Plant growth}} - \underbrace{bu}_{\text{Plant loss}} + \underbrace{\frac{\partial^2 u}{\partial x^2}}_{\text{Plant dispersal}} \\ \frac{\partial w}{\partial t} &= \underbrace{a}_{\text{Rainfall}} - \underbrace{w}_{\text{Evaporation}} - \underbrace{wu^2}_{\text{Uptake by plants}} + \underbrace{\nu \frac{\partial w}{\partial x}}_{\text{Downhill flow}}\end{aligned}\tag{2.2}$$

The dimensionless parameters have clear biological meanings. The parameters a, b, ν control the level of rainfall, the level of evaporation and the the angle of the slope. Appropriate parameter values were chosen from field observations (Mauchamp, Rambal, and Lepart 1994; White 1970; Worral 2006) (Latter published in 1959).

$a_{tree} = 0.077 - 0.23$, $m_{tree} = 0.045$, $a_{grass} = 0.94 - 2.81$, $m_{grass} = 0.45$, $\nu = 182.5$. The model predicts that grass stripes will have wavelengths 8.1 – 28m in width and move 1.4 – 1.9m/yr. This project will take the parameters for grass, fixing both the level of evaporation $b = 0.45$, slope $\nu = 182.5$ and varying the level of rainfall. The solution will be defined as the following vector.

$$\mathbf{V}(x, t) = \begin{pmatrix} u(x, t) \\ w(x, t) \end{pmatrix}\tag{2.3}$$

Numerical simulation is crucial in understanding the long term dynamics of vegetative bands. The bands migrate uphill extremely slowly and therefore real world analysis is difficult and costly. The parameters and conditions can be easily adjusted for this model.

2.1 Locating the uniformly stable steady states

Finding the spatially uniform stable states will be the first step of the linear analysis. Spatial diffusion is ignored, finding the equilibrium points of the following equation:

$$\begin{aligned}\frac{\partial u}{\partial t} &= f(u, w) \\ \frac{\partial w}{\partial t} &= g(u, w)\end{aligned}\tag{2.4}$$

The non-linear reaction terms f, g model the reaction kinetics between either interacting variable (Maini et al. 2012). The vegetative density is controlled by a positive feedback loop, given by the non-linear (wu^2) term.

$$\begin{aligned}f(u, w) &= wu^2 - bu \\ g(u, w) &= a - w - wu^2\end{aligned}\tag{2.5}$$

The spatially uniform steady state will be the points (u_0, w_0) which satisfy $f(u_0, w_0) = g(u_0, w_0) = 0$. There are a maximum of three steady states depending on the parameters of the model. Firstly zero solutions of the function f will be searched for:

$$\begin{aligned}f(u, w) &= wu^2 - bu = 0 \\ u(wu - b) &= 0 \Rightarrow \\ u = 0 \quad \text{or} \quad u &= \frac{b}{w}\end{aligned}$$

Given that $u_0 = 0$, $g(0, w) = a - w = 0$; $(u_0, w_0) = (0, a)$ which is the spatially uniform desert steady state. The steady state has zero plant density and a surface water density equal to the level of rainfall. Solutions of the following form will now be searched for: $u = \frac{b}{w}$

$$\begin{aligned}g(u, w) &= a - w - wu^2 = 0 \\ a/w - 1 - u^2 &= 0 \quad \text{sub in}(u = \frac{b}{w}) \\ u^2 - \frac{a}{b}u + 1 &= 0 \Rightarrow \\ \left(u - \frac{a}{2b}\right)^2 &= \frac{a^2}{4b^2} - 1 \Rightarrow \\ u &= \frac{1}{2b} \left(a \pm \sqrt{(a^2 - 4b^2)}\right)\end{aligned}$$

In total there are three possible equilibrium points for the spatially uniform model:

$$\begin{aligned}(u_0, w_0) &= (0, a) \\ (u_1, w_1) &= \left(\frac{1}{2b}(a + \sqrt{a^2 - 4b^2}), \frac{2b^2}{(a + \sqrt{a^2 - 4b^2})}\right) \\ (u_2, w_2) &= \left(\frac{1}{2b}(a - \sqrt{a^2 - 4b^2}), \frac{2b^2}{(a - \sqrt{a^2 - 4b^2})}\right)\end{aligned}$$

In order for $(u_1, w_1), (u_2, w_2)$ to be real solutions then it is required that $a^2 - 4b^2 > 0$. As both a, b must be positive then it suffices to show that $a > 2b$. At $a = 2b$ then $(u_1, w_1) = (u_2, w_2)$.

Non-desert spatially uniform steady states exists if and only if the level of rainfall $a \geq 2b$. The code is written with *MATLAB* (MATLAB 2022).

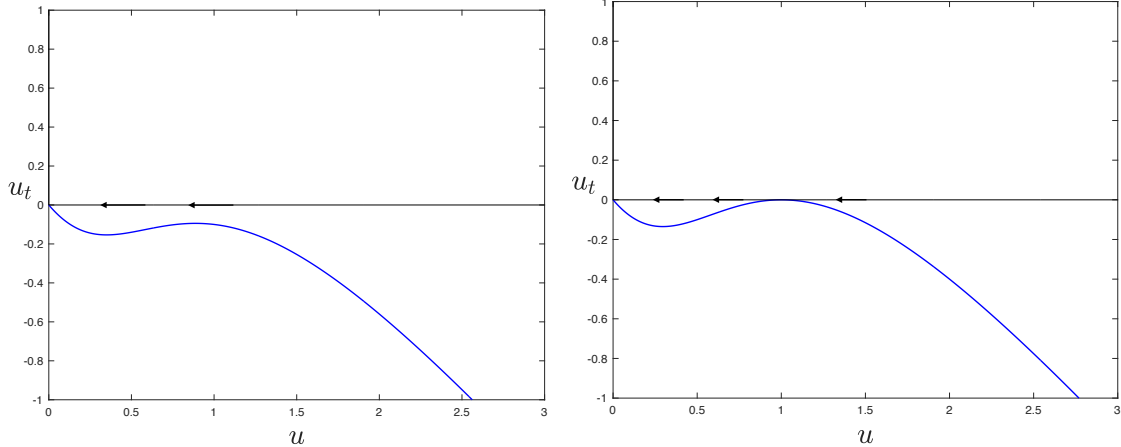


Figure 2.1: The left plots the partial derivative for the vegetative density given $a < 2b$. The second right is the case in which $a = 2b$; $(u_1, w_1) = (u_2, w_2)$. There will be three points for $u_t = 0$ for higher values of a .

Uniform steady state stability analysis

Uniform perturbations (\hat{u}, \hat{w}) will be added to the steady state in order to analyse the linear stability of the spatially uniform Klausmeier model (see 2.5).

$$\begin{aligned} u &= u_{eq} + \hat{u} \\ w &= w_{eq} + \hat{w} \end{aligned} \tag{2.6}$$

The reaction functions f, g will be linearised at the equilibrium point using Taylor-expansion. Note the following substitutions; $u - u_{eq} = \hat{u}$ and $w - w_{eq} = \hat{w}$:

$$\begin{aligned} f(u, w) &= f_u(u_{eq}, w_{eq})\hat{u} + f_w(u_{eq}, w_{eq})\hat{w} + O(2) \\ g(u, w) &= g_u(u_{eq}, w_{eq})\hat{u} + g_w(u_{eq}, w_{eq})\hat{w} + O(2) \end{aligned} \tag{2.7}$$

The linearised model will be substituted back into the spatially homogeneous model, Equation 2.4:

$$\begin{aligned} \hat{u}_t &= f_u(u_{eq}, w_{eq})\hat{u} + f_w(u_{eq}, w_{eq})\hat{w} + O(2) \\ \hat{w}_t &= g_u(u_{eq}, w_{eq})\hat{u} + g_w(u_{eq}, w_{eq})\hat{w} + O(2) \end{aligned} \tag{2.8}$$

Taking $\hat{\mathbf{V}} = (\hat{u}, \hat{w})^t$, equation 2.8 will be expressed in matrix form; $\hat{\mathbf{V}}_t = A\hat{\mathbf{V}}$. Note the partial derivatives are defined at the equilibrium point (u_{eq}, w_{eq}) .

$$\begin{pmatrix} \hat{u}_t \\ \hat{w}_t \end{pmatrix} = \begin{pmatrix} f_u & f_w \\ g_u & g_w \end{pmatrix} \begin{pmatrix} \hat{u} \\ \hat{w} \end{pmatrix} = \begin{pmatrix} 2u_{eq}w_{eq} - b & u_{eq}^2 \\ -2u_{eq}w_{eq} & -u_{eq}^2 - 1 \end{pmatrix} \begin{pmatrix} \hat{u} \\ \hat{w} \end{pmatrix} \tag{2.9}$$

The eigenvalues of the Jacobian matrix (A) fixed at each equilibrium point will determine the stability. Setting $A\hat{\mathbf{V}} = \lambda\hat{\mathbf{V}}$; the vector grows with linear growth rate λ . The sign of the eigenvalue will determine the stability of the spatially uniform steady state.

$$|A - \lambda I| = \begin{vmatrix} f_u - \lambda & f_w \\ g_u & g_w - \lambda \end{vmatrix} = 0 \tag{2.10}$$

In order for the spatially homogeneous system to be stable then the $\det(A) > 0$ and $\text{trace}(A) < 0$; which guarantees eigenvalues of negative real part.

$$\begin{aligned} f_u + g_w &< 0 \\ f_u g_w - g_u f_w &> 0 \end{aligned} \tag{2.11}$$

For the desert steady state $(0, a)$, $\det(A) = b > 0$ and $\text{Trace}(A) = -b - 1 < 0$. Hence the desert steady state is always stable.

For the non-desert spatially uniform steady states $(u_1, w_1), (u_2, w_2)$ then both $\det(A) = b(3u^2 - 1)$ and $\text{Trace}(A) = b + u^2 - 1$. For this (u_1, w_1) is always a stable equilibrium point, and (u_2, w_2) is an unstable saddle node (as the determinant is negative). The perturbations of the system will grow as follows:

$$\hat{\mathbf{V}} = \hat{\mathbf{V}}_1 e^{\lambda_1 t} + \hat{\mathbf{V}}_2 e^{\lambda_2 t}$$

The factors $\hat{\mathbf{V}}_{1,2}$ are the corresponding eigenvectors for the eigenvalues. There are two spatially uniform steady states; The desert and non-desert state given respectively below.

$$(0, a), \left(\frac{1}{2b} (a + \sqrt{a^2 - 4b^2}), \frac{2b^2}{(a + \sqrt{a^2 - 4b^2})} \right)$$

Using the numerical continuation package *MATCONT* (hilmeijer and willygovaerts 2021) the stability and location of the equilibria can be plotted.

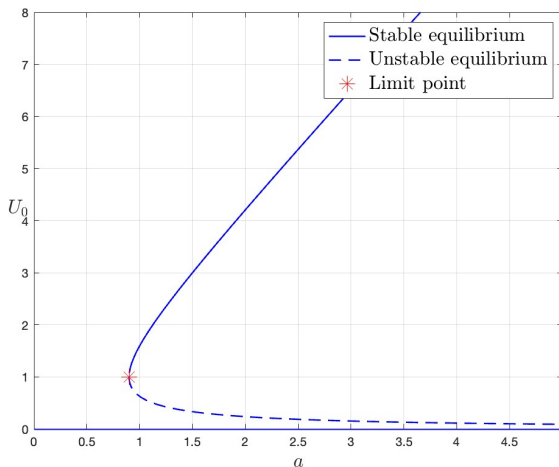


Figure 2.2: Bifurcation diagram for $b = 0.45$. The limit point occurs at $a = 0.9$ which marks the transition from one to three spatially homogeneous steady states. The non-zero solid line maps the stable vegetative steady state (u_1, w_1) , the dashed line maps the unstable vegetative steady state (u_2, w_2) . The line at $u_0 = 0$ maps the vegetative steady state

The system is bistable for $a \geq 2b$, there will be two attracting states which ultimately control the dynamics of the system. The parameter $a = 2b$ will be referred to as the *tipping point* (Rietkerk, Dekker, et al. 2004) or *limit point* marking the transition from one stable equilibrium points to two. A critical transition will occur when the initial conditions are forced into the basin of attraction of the spatially homogeneous desert steady state (Scheffer et al. 2001b; Rietkerk, Dekker, et al. 2004). As the rainfall reduces a smaller perturbation may result in the initial conditions being forced into the undesirable basin of attraction. The system will be less resilient to change (Holling 1973).

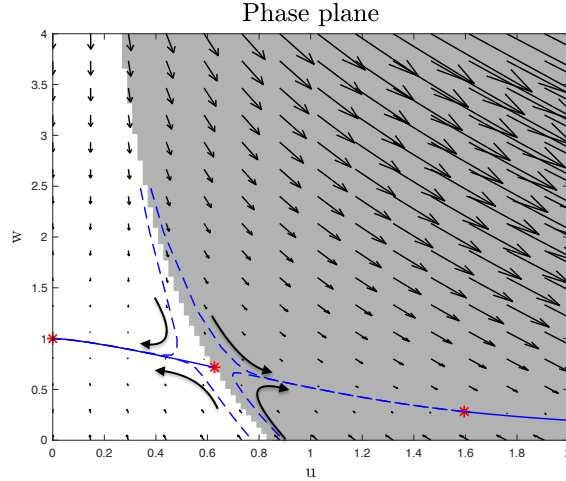


Figure 2.3: $a = 1, b = 0.45$. The phase plane for the spatially homogeneous model. Initial conditions within the grey region will converge to the spatially uniform steady state (u_1, w_1) , otherwise it will converge to the desert steady state (u_0, w_0)

Figure 2.3 is the phase plane of the spatially uniform model given that the rainfall is relatively close to the tipping point. The initial conditions in the grey region will converge to (u_1, w_1) otherwise it will converge to the desert steady state (u_0, w_0) . The separatrix divides either mode of behaviour.

2.2 Stability analysis of spatially uniform equilibria with non-uniform perturbations

Only the spatially homogeneous system has been considered, painting only half the picture. The spatial part of the system models the dispersion of water and plants over space leading to the complex interactions, spatial instability and uphill propagation. In the presence of diffusion spatial perturbations grow over time forming pattern via *Diffusion-advection-driven instability*, (P.K. Maini and Myerscough 1997; Maini et al. 2012). Only the plants will diffuse over space and hence the overall system is similar but not identical to the chemical models studied by Turing. The development of patterns will occur at the vegetative steady state close to the tipping point (Rietkerk, Dekker, et al. 2004). Only Certain wave modes will grow over time bridging the gap between the two spatially uniform steady states (Rietkerk, Bastiaansen, Banerjee, Jvan de Koppel, et al. 2021).

The possibility of diffusion-driven instability will be considered at both the stable desert steady state (u_0, w_0) and the vegetative steady state (u_1, w_1) . The partial derivatives f_u, f_w, g_u, g_w , see equation 2.9, are functions defined at the spatially uniform steady state. The spatial parts of Klausmeier equation will be reintroduced to the linearised equation 2.9. The following Turing analysis used the methods from *Mathematical Biology II: Spatial Models and Biomedical Application* (Murray 2003). This approach for the reaction diffusion-advection problem is similar to the models studied by Turing.

$$\begin{pmatrix} \hat{u}_t \\ \hat{w}_t \end{pmatrix} = \begin{pmatrix} f_u & f_w \\ g_u & g_w \end{pmatrix} \begin{pmatrix} \hat{u} \\ \hat{w} \end{pmatrix} + \overbrace{\begin{pmatrix} 1 & 0 \\ 0 & 0 \end{pmatrix} \begin{pmatrix} \hat{u}_{xx} \\ \hat{w}_{xx} \end{pmatrix}}^{\text{Spatial part}} + \begin{pmatrix} 0 & 0 \\ 0 & \nu \end{pmatrix} \begin{pmatrix} \hat{u}_x \\ \hat{w}_x \end{pmatrix} \quad (2.12)$$

The solution for the perturbation will be a function of both time and space. Importantly the solution will be spatially non-uniform of a particular frequency and given in exponential form (Murray 2003):

$$\hat{\mathbf{V}}(x, t) = \boldsymbol{\alpha} \exp(ikx + \lambda t) \quad (2.13)$$

Spatial patterns will form of a particular mode (or frequency),(Klausmeier 1999; Rietkerk, Boerlijst, et al. 2002; Thiery, D'Herbes, and C. Valentin 1995) and given by the wavenumber k . The

wavenumber determines the spatial frequency of the solution and λ the growth rate. The vector α is the corresponding eigenvector of the solution.

The wavenumber is inversely proportional to the wavelength $\frac{2\pi}{k} = \gamma$. The complex exponential can be expanded as the following:

$$\hat{\mathbf{V}}(x, t) = \alpha e^{\lambda t} (\cos(kx) + i \sin(kx)) \quad (2.14)$$

The growth rate of the solution will depend on the spatial frequency. The eigenvalue can therefore be written as a function of the wavenumber ($\lambda(k)$) and called the *dispersion relation* (Murray 2003).

The relative derivatives of the candidate solution can be taken as follows: $\hat{\mathbf{V}}_t = \lambda \hat{\mathbf{V}}$, $\hat{\mathbf{V}}_x = ik\hat{\mathbf{V}}$, $\hat{\mathbf{V}}_{xx} = -k^2\hat{\mathbf{V}}$. These values will be substituted back into equation 2.12; appropriate rearranging and cancelling of the exponential terms yields the following matrix equation:

$$(M - \lambda I)\alpha = 0 \quad (2.15)$$

The matrix M depends on the equilibrium point (As the partial derivatives are defined here) and k . The matrix will expressed with respect to both:

$$M_{eq}(k) = \begin{pmatrix} f_u - k^2 & f_w \\ g_u & g_w + ik\nu \end{pmatrix} \quad (2.16)$$

In order for the solution $\hat{\mathbf{V}}$ to have non-trivial solutions then the left part of equation 2.15 must be equal to zero, forcing $\text{Det}(M_{eq}(k) - \lambda I) = 0$. The spectrum of eigenvalues if given by:

$$\sigma(M_{eq}(k)) = \{\lambda \in \mathbb{C} : \det(M_{eq}(k) - \lambda I) = 0\} \quad (2.17)$$

The set of possible eigenvalues are partitioned into the following subsets:

$$\begin{aligned} \sigma_s &= \{\lambda \in \sigma(M_{eq}(k)) : \text{Re}(\lambda) < 0\} & \sigma_c &= \{\lambda \in \sigma(M_{eq}(k)) : \text{Re}(\lambda) = 0\} \\ \sigma_u &= \{\lambda \in \sigma(M_{eq}(k)) : \text{Re}(\lambda) > 0\} \end{aligned} \quad (2.18)$$

The determinant can be written as a quadratic equation:

$$\lambda^2 + \lambda r(k) + h(k) = 0 \quad (2.19)$$

In which the coefficients are given by the following:

$$\begin{aligned} r(k) &= k^2 - f_u - g_w - ik\nu \\ h(k) &= -k^2 g_w + i(k\nu f_u - k^3\nu) + f_u g_w - g_u f_w \end{aligned} \quad (2.20)$$

The two dispersion relations ($\lambda(k)$) will be the roots of the quadratic equation. The dispersion relation is crucial in understanding the frequencies which grow over time. There will be two modes of behaviour, the unstable range of wavenumbers $\text{Re}\lambda(k) > 0$ and stable range $\text{Re}\lambda(k) < 0$.

The linearly unstable perturbations should grow exponentially over time before being eventually bounded by the non-linear reaction terms f, g forming a stable spatially inhomogeneous solution (Murray 2003; P.K. Maini and Myerscough 1997).

2.2.1 Boundary conditions

By applying periodic boundary conditions Turing derived the conditions required for diffusion driven instability (Maini et al. 2012). Over a finite domain the periodic boundary conditions impose restrictions on the allowable set of possible wavenumbers k , forming a discrete set. The system is to be defined on a circular domain $[0, \ell]$, A unit cell (Shuguang 2008) in order to emulate an infinite domain. The following must be satisfied:

$$\hat{\mathbf{V}}(0, t) = \hat{\mathbf{V}}(\ell, t) \quad (2.21)$$

Substituting in the exponential function and cancelling terms gives this following requirement.

$$\begin{aligned} \exp(ik\ell) &= 1 \Rightarrow \\ \cos(k\ell) &= 1 \end{aligned} \quad (2.22)$$

The expression $\cos(x) = 1$ is true given $x = 2\pi j$ for $\forall j \in \mathbb{N} \cup 0$. The wavenumber k must take discrete values with respect to the length of the spatial domain:

$$k_j = \frac{2\pi j}{\ell}, \quad j = 0, 1, 2, 3, \dots \quad (2.23)$$

The set $\mathbb{K}(\ell)$ will contain the discrete class of wavenumbers. The set will depends on the length of the domain.

$$\mathbb{K}(\ell) = \left\{ \frac{2\pi j}{\ell} : j \in \mathbb{N} \cup 0 \right\} \quad (2.24)$$

The wavenumber will generally be expressed with respect to the index j and written with the relevant subscript, $k_j = \frac{2\pi j}{\ell}$. The corresponding spatial period of the wave is $\gamma = \frac{2\pi}{k}$. Given that ℓ is an infinite domain then the wavenumbers will span the positive real numbers however this cannot be implemented numerically. The wavelength is restricted to the length of the finite domain. As stated before the discrete class of wavenumbers encompass two modes of behaviour depending on the sign of the real part of the dispersion relation $\lambda(k)$.

Diffusion driven instability will cause initial patterns to grow for $k \in \mathbb{K}$ given that the dispersion relation $\lambda(k) \in \sigma_u(M_{eq}(k))$, the unstable spectrum of eigenvalues. The set $\mathbb{K}(\ell) \subset \mathbb{K}(\infty)$ taking discrete points at equal intervals along the real number line.

2.2.2 The Desert steady state

Non-linear perturbations of the desert steady state should grow given that $\sigma_u(M_{(u_0, w_0)}(k)) \neq \phi, \forall k \in \mathbb{K}(\ell)$. At this equilibrium the partial derivatives are always equal to the following: $(f_u, f_w, g_u, g_w) = (-b, 0, 0, -1)$. The relevant matrix will be expressed:

$$M_{(u_0, w_0)}(k) = \begin{pmatrix} -b - k^2 & 0 \\ 0 & -1 + ik\nu \end{pmatrix} \quad (2.25)$$

The determinant and trace of the matrix will determine the stability given the presence of diffusion; $\text{Det}(M_{(u_0, w_0)}(k)) = (b + k^2 - i(\nu B + k^2\nu))$, $\text{Trace}(M_{(u_0, w_0)}(k)) = -b - k^2 - 1 + ik\nu$. Ignoring the imaginary parts the determinant is always positive and the trace is always negative, as $b, k, \nu > 0$. At this equilibrium $\sigma_u(M) = \phi$. For all possible wavenumbers then the real part of the dispersion relation is negative. Referring back to 2.13 the initial perturbation will grow over time in the model form.

$$\hat{\mathbf{V}}(x, t) = \alpha \exp(ikx + \lambda t)$$

As all eigenvalues have negative real part then the perturbations will in fact shrink over time. This highlights the stability of the desert steady state, it is black hole for the growth of vegetation. There

is no possibility of vegetative patterns forming from small initial growths. The initial conditions must be forced into the vegetative steady states basin of attraction (see Figure 2.3) in order for the behaviour to change.

2.2.3 Vegetative steady state

For the vegetative steady state (u_1, w_1) Turing instability will occur over a range of a for a fixed evaporation constant. There are possible levels of rainfall such that $\sigma_u(M_{(u_1, w_1)}) \neq \phi$ for $k \in \mathbb{K}(\ell)$ (of a sufficiently large domain size) over a range of a .

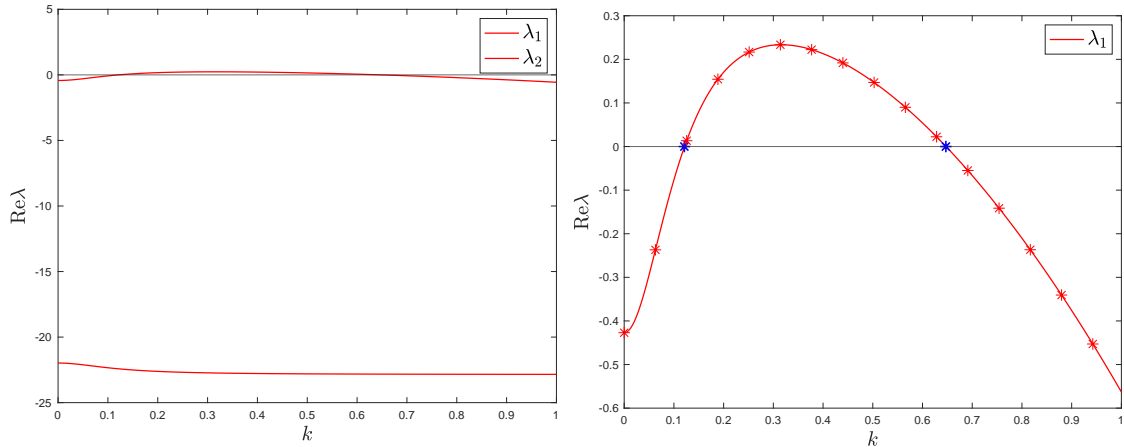


Figure 2.4: The graph of the dispersion relation for $A = 2.2, B = 0.45, \nu = 182.5$. Eigenvalue λ_2 has negative real part. The real part of λ_1 is positive for $k \in (0.12, 0.65)$. The real part of the eigenvalue peaks at $k = 0.31$. The distinct wavenumbers have been plotted for $\ell = 100$ and zoomed in at the dominant eigenvalue

The real part of the dispersion relation $\lambda = \lambda(k)$ is plotted for a range of wavenumbers for both the infinite and finite domain (which restricts k to a discrete class of possible values). The graph is informative as it demonstrates the exact spatial frequencies which should grow over time. The dispersion relation has a range in which $\text{Re}(\lambda(k)) > 0$ and a particular wavenumber k_m which has the highest growth rate. It's clear that a large domain size is important in order to capture necessary k values. If the domain size is too small then there may be no allowable wavenumbers k to be driven unstable (Murray 2003).

The dispersion relation ($\lambda(k)$) is complex at the vegetative steady state and attributed to the advection component of the model (Klausmeier 1999). The consequence of this can be analysed by splitting the eigenvalue into complex form; $\lambda(k) = \mu(k) + i\psi(k)$:

$$\begin{aligned}\hat{\mathbf{V}}(x, t) &= \alpha \exp(i k x + (\mu(k) + i\psi(k)) \cdot t) \Rightarrow \\ \hat{\mathbf{V}}(x, t) &= \alpha \exp(i(kx + \psi(k)t) + \mu(k)t) \Rightarrow \\ \hat{\mathbf{V}}(x, t) &= \alpha \exp(\mu(k)t) (\cos(kx + \psi(k)t) + i \sin(kx + \psi(k)t))\end{aligned}\tag{2.26}$$

The real part of the eigenvalue will correspond to the spatial frequency of the wave and the imaginary part the speed of the stable travelling wave solution.

As previously mentioned (b, ν) will be respectively set to $(0.45, 182.5)$ inline with plausible parameters for grass (Klausmeier 1999). The level of rainfall (a) will be varied over an appropriate range. The set of wavenumbers which have a positive growth rate for the domain size (ℓ) and rainfall level (a) is given by the following:

$$\begin{aligned}\mathbb{K}_+(\ell, a) &= \{\forall k \in \mathbb{K}(\ell) \mid \lambda(k) \in \sigma_u(M_{eq}(k))\} \\ \mathbb{K}_+(\ell) &\subseteq \mathbb{K}(\ell)\end{aligned}\tag{2.27}$$

Diffusion-driven instability of non-uniform spatial perturbations occurs up until a critical level of rainfall (Klausmeier 1999). The high level of rainfall sustains a high density of vegetation in which perturbations fail to grow into patterns. This threshold was acknowledged by Klausmeier and later being referred as the Turing-Hopf bifurcation (Stelt et al. 2013). The positive set of wavenumbers can be expressed as the following closed set:

$$\mathbb{K}_+(A, \ell) = \bigcup_{i=n}^m \frac{2\pi i}{\ell} \quad (2.28)$$

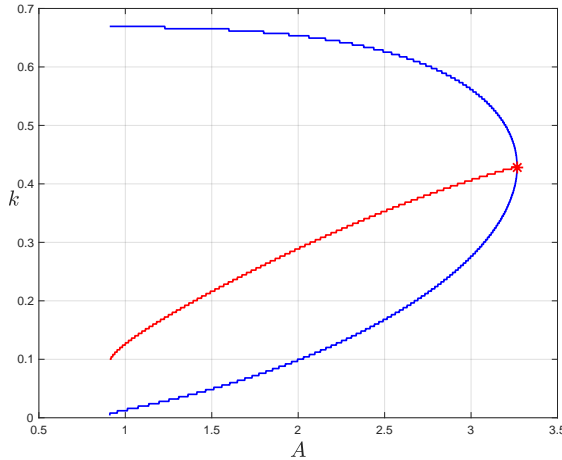


Figure 2.5: $b = 0.45, \nu = 182.5, \ell = \infty$. The minimum and maximum wavenumber for spatial instability relative to parameter a . The red central line plots the k value yielding the largest eigenvalue. The Turing-Hopf bifurcation occurs at $a = 3.27$

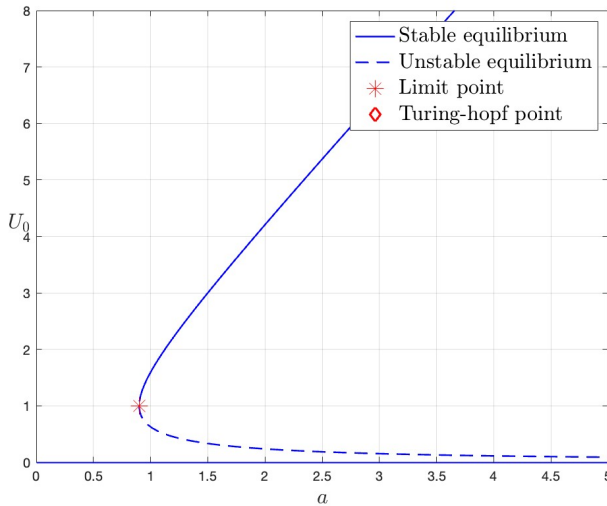


Figure 2.6: The location of the equilibrium points with the Turing-hopf bifurcation labelled

The Turing-Hopf bifurcation marks the point at which spatial patterns will cease to occur as a is increased. Figure 2.5 represents the upper and lower limits of the set $\mathbb{K}_+(a)$ for a varying parameter a and is noted for its similarity to Figure 1.7. In this figure $a > 2b$ as the stable vegetative steady state does not exist otherwise. The range of possible wave numbers which yield eigenvalues of positive real part shrinks as the value of a increases as the possible patterns to form becomes limited as the level of rainfall increases. The dominant wavenumber increases as the level of rainfall increases which implies that a pattern of a shorter wavelength will be favoured (J.A Sherratt 2007). This

2.2. STABILITY ANALYSIS OF SPATIALLY UNIFORM EQUILIBRIA WITH NON-UNIFORM PERTURBATIONS

supports the field observations, given in Figure 1.3 Valentin, d'Herbes, and Poesen 1999 and the very early observation of *Brousee tigrée* (White 1970). This also supports the analysis given by Klausmeier (See Figure 1.4).

The lower bound is simply when there is no spatially uniform steady state to perturb from. However this does not negate the possibility that vegetative patterns will exist for rainfall $a < 2b$. This introduces the idea that spatial patterns continue to exist below for lower levels of rainfall and a 'signal of resilience' (Rietkerk, Bastiaansen, Banerjee, Koppell, et al. 2021)against critical transition. Numerical simulation of the partial differential model must be implemented in order to map the patterns below the tipping point and track the survival.

Chapter 3

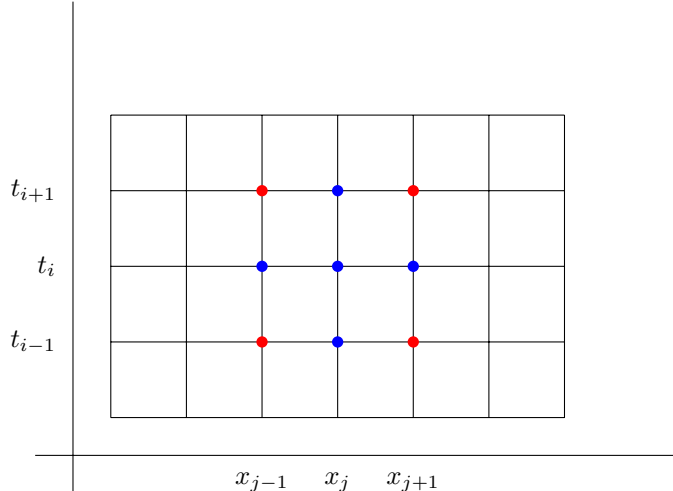
PDE simulation

3.1 Finite-difference approximation

The Partial differential model will be simulated over the finite spatial domain over time to observe the development and subsequent migration of the spatial stripes. The code will be written in *MATLAB*(MATLAB 2022). For the numerical simulation both the temporal and spatial domain must be discretised into a finite number of grid points. The spatial domain $x = [0, \ell]$ will be partitioned into n grid points; The temporal domain $t = [0, T]$ will be partitioned into m grid points (Kharab and Guenther 2002). Each grid point will be denoted x_j for $j = 1, \dots, n$ and t_i for $i = 1, \dots, m$. The points (x_j, t_i) are defined as the following

$$\begin{aligned} x_j &= (j - 1)\Delta x \quad \text{for } i = 1, \dots, n \\ t_i &= (i - 1)\Delta t \quad \text{for } j = 1, \dots, m \end{aligned} \tag{3.1}$$

The term (u_j^i, w_j^i) will denote the numerical solution at the grid point (t_i, x_j) . The true analytic solution will be given by $(u(t_i, x_j), w(t_i, x_j))$. The following diagram graphically represents this spatiotemporal grid.



Each grid point has both a discrete time and location in space. The grid can be considered cylindrical; the solution wraps around the spatial domain. The formal derivative of a function with respect to x is given by the following:

$$f_x(x) = \lim_{\Delta x \rightarrow 0} \frac{f(x + \Delta x) - f(x)}{\Delta x} \tag{3.2}$$

The partial derivatives of the numerical solution will be calculated at each grid point:

$$\begin{aligned} u_t(x_j, t_i) &= \frac{u(x_j, t_{i+1}) - u(x_j, t_i)}{\Delta t} + O(\Delta t) \\ u_x(x_j, t_i) &= \frac{u(x_{j+1}, t_i) - u(x_j, t_i)}{\Delta x} + O(\Delta x) \\ u_{xx}(x_j, t_i) &= \frac{u(x_{j+1}, t_i) - 2u(x_j, t_i) + u(x_{j-1}, t_i)}{\Delta x^2} + O(\Delta x^2) \end{aligned} \quad (3.3)$$

The solution will be written in vector form for each timestep i across the entire spatial domain:

$$\begin{aligned} \mathbf{u}^i &= [u_1^i, u_2^i, \dots, u_n^i] \\ \mathbf{w}^i &= [w_1^i, w_2^i, \dots, w_n^i] \end{aligned} \quad (3.4)$$

3.2 Stability of different numerical methods

The Klausmeier model is a non-linear diffusion-advection problem and will be numerically solved using different finite-difference methods. The numerical scheme must be stable and of relatively high accuracy. To be a numerically stable scheme then the solutions error should not grow over time. In order to study the stability the non-linear terms will be removed with the diffusion equation considered:

$$\frac{\partial u}{\partial t} = \frac{\partial^2 u}{\partial x^2} \quad (3.5)$$

The resulting partial differential is the heat equation (Wendt and Anderson 2008).

3.2.1 Explicit Euler method

The diffusion term for the explicit Euler method will be defined at the t^i (explicit) timestep. The diffusion term will be approximated using the second order centered difference method (equation 3.3) giving the following recurrence relation.

$$\frac{u_j^{i+1} - u_j^i}{\Delta t} = \frac{u_{j+1}^i - 2u_j^i + u_{j-1}^i}{\Delta x^2} \quad (3.6)$$

After rearrangement the forward stepping process is given by:

$$u_j^{i+1} = u_j^i + \frac{\Delta t}{\Delta x^2} (u_{j+1}^i - 2u_j^i + u_{j-1}^i) \quad (3.7)$$

In order to understand the stability the round-off error will be taken: $\epsilon_j^i = u(x_j, t_i) - u_j^i$, the error between the true and numerically approximated solution. The Von-Neumann approach (Wendt and Anderson 2008) is to approximate the error $\epsilon_j^n \approx \alpha^i e^{ikx_j}$ by considering the single Fourier mode. The following condition must be followed in order to be stable:

$$\left| \frac{\epsilon_j^{i+1}}{\epsilon_j^i} \right| = |\alpha| < 1$$

The amplification factor (α) must be smaller than 1. Substituting the exponential approximation into the explicit scheme yields:

$$\alpha^{i+1} e^{ikx_j} = \alpha^i e^{ikx_j} + \frac{\Delta t}{\Delta x^2} (\alpha^i e^{ikx_{j+1}} - 2\alpha^i e^{ikx_j} + \alpha^i e^{ikx_{j-1}})$$

Dividing through by αe^{ikx_j} and rearranging:

$$\begin{aligned}
 \alpha &= 1 + \frac{\Delta t}{\Delta x^2} (e^{ik\Delta x} - 2 + e^{-ik\Delta x}) \\
 \alpha &= 1 + \frac{2\Delta t}{\Delta x^2} (\cos(k\Delta x) - 1) \Rightarrow \\
 1 - \frac{4\Delta t}{\Delta x^2} &\leq \alpha \leq 1 \Rightarrow \\
 1 - \frac{4\Delta t}{\Delta x^2} &\geq -1
 \end{aligned} \tag{3.8}$$

The explicit Euler method for the heat equation will be stable given that $\Delta t \leq \frac{\Delta x^2}{2}$. The size of the timestep must be kept proportional to the inverse square of the spatial step. This is problematic as in order to have relatively high spatial accuracy the timestep must be kept extremely small. The explicit Euler method is straight forward to numerically execute as all the explicit terms are on the right side of the equation and hence there are no unknowns. This explains why the stability analysis for the diffusion term was used rather than advection term.

3.2.2 Implicit Euler method

The implicit method uses the same finite difference approximations however the spatial derivative is defined at the implicit t^{i+1} timestep giving the following recurrence relation:

$$\frac{u_j^{i+1} - u_j^i}{\Delta t} = \frac{u_{j+1}^{i+1} - 2u_j^{i+1} + u_{j-1}^{i+1}}{\Delta x^2} \tag{3.9}$$

This method is again of first order accuracy with respect to the timestep and second order with respect to the spatial steps (For the heat equation).

$$u_j^{i+1} = u_j^i + \frac{\Delta t}{\Delta x^2} (u_{j+1}^{i+1} - 2u_j^{i+1} + u_{j-1}^{i+1}) \tag{3.10}$$

As before substituting the exponential approximation yields the following:

$$\alpha^{i+1} e^{ikx_j} = \alpha^i e^{ikx_j} + \frac{\Delta t}{\Delta x^2} (\alpha^{i+1} e^{ikx_{j+1}} - 2\alpha^{i+1} e^{ikx_j} + \alpha^{i+1} e^{ikx_{j-1}})$$

Dividing through by $\alpha^i e^{ikx_j}$:

$$\begin{aligned}
 \alpha &= 1 + \frac{\alpha \Delta t}{\Delta x^2} (e^{ik\Delta x} - 2 + e^{-ik\Delta x}) \Rightarrow \\
 \alpha &= \frac{1}{1 + \frac{2\Delta t}{\Delta x^2} (1 - \cos(k\Delta x))}
 \end{aligned} \tag{3.11}$$

The denominator of equation 3.11 is strictly positive and so $0 < \alpha \leq 1$. The numerical method is unconditionally stable when solving the one-dimensional heat equation. Iterating the method over time is more difficult to execute as there are unknown implicit terms on the right side of the equation. At each time evolution step an $N \times N$ matrix must be inverted which is computational expensive.

3.2.3 The Crank-Nicolson method

The Crank-Nicolson method is a favoured numerical scheme for solving the heat equation (Crank and Nicolson 1996, introduced in 1947). The method is both unconditionally stable and second order accurate. The numerical method was not explicitly stated in the Klausmeier paper, however *semi-implicit* method was used (J.A Sherratt 2013). This method has been implemented in areas of financial mathematics for example numerically solving the Black-Scholes equation (Duffy 2004). The method combines the implicit and explicit methods to approximate the diffusion operator. The method is second order accurate with respect to both the spatial and temporal step (For the heat equation), hence the error can be expressed:

$$\epsilon = O(\Delta x^2) + O(\Delta t^2)$$

$$\frac{u_j^{i+1} - u_j^i}{\Delta t} = \frac{u_{j+1}^i - 2u_j^i + u_{j-1}^i}{2\Delta x^2} + \frac{u_{j+1}^{i+1} - 2u_j^{i+1} + u_{j-1}^{i+1}}{2\Delta x^2} \quad (3.12)$$

Forward-stepping the time derivative results in the following:

$$u_j^{i+1} = u_j^i + \frac{\Delta t}{2\Delta x^2} (u_{j+1}^{i+1} + u_{j-1}^{i+1} + u_{j+1}^i + u_{j-1}^i - 2u_j^{i+1} - 2u_j^i)$$

Taking the round off error as before.

$$\alpha^{i+1} e^{ikx_j} = \alpha^i e^{ikx_j} \left(1 + \frac{\Delta t}{2\Delta x^2} (\alpha e^{ik\Delta x} + \alpha^{-ik\Delta x} + e^{ik\Delta x} + e^{-ik\Delta x} - 2\alpha - 2) \right) \quad (3.13)$$

$$\begin{aligned} \alpha &= 1 + \frac{\Delta t}{\Delta x^2} (\alpha + 1) (\cos(k\Delta x) - 1) \\ \alpha (1 + \frac{\Delta t}{\Delta x^2} (1 - \cos(k\Delta x))) &= 1 - \frac{\Delta t}{\Delta x^2} (1 - \cos(k\Delta x)) \end{aligned} \quad (3.14)$$

Setting $Q = 1 - \cos(k\Delta x)$, bounding $0 \leq Q \leq 2$. Setting $P = \frac{\Delta t}{\Delta x^2} Q$. Then:

$$\alpha = \frac{1 - P}{1 + P}$$

And for $\forall p \in (0, \infty)$ then $\alpha \in (-1, 1)$; the method is unconditionally stable for the heat equation. However given that $\frac{\Delta t}{\Delta x^2} \gg 0$ then:

$$\lim_{p \rightarrow \infty} \alpha = \frac{-P}{P} = -1$$

In this case the numerical solution would oscillate over time. There is still a restriction on the size of Δx such that the fraction, $\frac{\Delta t}{\Delta x^2}$, remains small.

3.3 Discretisation of the differential operator

The spatial operator is a product of implicit and explicit terms which must be separated via matrix inversion, the numerical scheme will be more involved than the simple explicit Euler method (but of higher accuracy). The non-linear terms of the equation will be disregarded at first focusing only on the spatial operators.

$$\begin{aligned} \frac{\partial u}{\partial t} &= \frac{\partial^2 u}{\partial x^2} \\ \frac{\partial w}{\partial t} &= \nu \frac{\partial w}{\partial x} \end{aligned} \quad (3.15)$$

Taking $\mathbf{u}^i = [u_1^i, \dots, u_n^i]$, $\mathbf{w}^i = [w_1^i, \dots, w_n^i]$ then using finite-difference approximation the numerical solution will be of the following form: $\mathbf{u}_t = D_u \mathbf{u}$, $\mathbf{w}_t = D_w \mathbf{w}$. The matrices are of $n \times n$ dimension and contain the relevant finite-difference approximation elements, see equations 3.3.

$$\underbrace{\frac{\partial}{\partial t} \begin{bmatrix} \mathbf{u}^i \\ u_1^i \\ u_2^i \\ \vdots \\ u_n^i \end{bmatrix}}_{D_u} = \underbrace{\begin{bmatrix} -2\Delta x^{-2} & \Delta x^{-2} & 0 & \dots & \Delta x^{-2} \\ \Delta x^{-2} & -2\Delta x^{-2} & \Delta x^{-2} & \dots & 0 \\ 0 & \Delta x^{-2} & -2\Delta x^{-2} & \Delta x^{-2} & \dots \\ \ddots & \ddots & \ddots & \ddots & \ddots \\ \Delta x^{-2} & 0 & \dots & \Delta x^{-2} & -2\Delta x^{-2} \end{bmatrix}}_{D_u} \begin{bmatrix} \mathbf{u}^i \\ u_1^i \\ u_2^i \\ \vdots \\ u_n^i \end{bmatrix} \quad (3.16)$$

The matrix D_u has terms $(-2\Delta x^{-2}, \Delta x^{-2}, \Delta x^{-2})$ for the leading diagonal, subdiagonal and superdiagonal respectively. There are additional terms Δx^{-2} at $(D_u)_{1,n}$ and $(D_u)_{n,1}$ to account for the circular domain. At each grid point the following scheme is implemented:

$$\frac{\partial u_j^i}{\partial t} = \frac{u_{j-1}^i - 2u_j^i + u_{j+1}^i}{\Delta x^2}$$

For the second part of the model:

$$\underbrace{\frac{\partial}{\partial t} \begin{bmatrix} w_1^i \\ w_2^i \\ \vdots \\ w_n^i \end{bmatrix}}_{\mathbf{w}^i} = \underbrace{\begin{bmatrix} -\nu\Delta x^{-1} & \nu\Delta x^{-1} & 0 & \cdots & 0 \\ 0 & -\nu\Delta x^{-1} & \nu\Delta x^{-1} & \cdots & 0 \\ 0 & 0 & -\nu\Delta x^{-1} & \nu\Delta x^{-1} & \cdots \\ \ddots & \ddots & \ddots & \ddots & \ddots \\ \Delta x^{-1} & 0 & \cdots & 0 & -\nu\Delta x^{-1} \end{bmatrix}}_{D_w} \begin{bmatrix} u_1^i \\ u_2^i \\ \vdots \\ u_n^i \end{bmatrix} \quad (3.17)$$

The matrix D_w has terms $(-\nu\Delta x^{-1}, \nu\Delta x^{-1})$ on the leading diagonal and superdiagonal respectively. There are no terms on the subdiagonal as the first order spatial operator does not depend on the previous spatial step. There is an additional term $\nu\Delta x^{-1}$ at $(D_w)_{n,1}$ to account for the circular domain. At each grid point the following scheme is implemented. Note this advection term is of order one spatial accuracy.

$$\frac{\partial w_j^i}{\partial t} = \frac{u_{j+1}^i - u_j^i}{\Delta x}$$

The partial derivatives are approximated by the direct neighbouring spatial grid point. The first and last spatial points are connected setting $u_0^i = u_n^i$.

The reaction terms $f(u, w), g(u, w)$ must now be incorporated into the numerical model. Taking \mathbf{a} to be a $N \times 1$ vector of values a . Using element-wise multiplication the vector $\mathbf{F}^i, \mathbf{G}^i$ will contain all the reaction terms at each spatial step at the corresponding timestep.

$$\begin{aligned} \mathbf{F}(\mathbf{u}^i, \mathbf{w}^i) &= \mathbf{w}^i \circ \mathbf{u}^i \circ \mathbf{u}^i - b\mathbf{u}^i \\ \mathbf{G}(\mathbf{u}^i, \mathbf{w}^i) &= \mathbf{a} - \mathbf{w}^i - \mathbf{w}^i \circ \mathbf{u}^i \circ \mathbf{u}^i \end{aligned} \quad (3.18)$$

The Semi-implicit method will be applied to the right side of the model (Equation 2.2)

$$\begin{aligned} \mathbf{u}^{i+1} &= \mathbf{u}^i + \frac{\Delta t}{2} (D_u \mathbf{u}^i + D_u \mathbf{u}^{i+1} + \mathbf{F}^i + \mathbf{F}^{i+1}) \\ \mathbf{w}^{i+1} &= \mathbf{w}^i + \frac{\Delta t}{2} (D_w \mathbf{w}^i + D_w \mathbf{w}^{i+1} + \mathbf{G}^i + \mathbf{G}^{i+1}) \end{aligned} \quad (3.19)$$

There is an obvious issue with the recurrence relation, equation 3.19, as the non-linear terms are defined at the unknown implicit timestep. The unknown terms must be approximated using the Euler-Heun method (Owkes 2015). For this the intermediate terms $\tilde{\mathbf{u}}^{i+1}, \tilde{\mathbf{w}}^{i+1}$ will be the intermediate approximations using the non-linear function at the explicit timestep.

$$\begin{aligned} \tilde{\mathbf{u}}^{i+1} &= \mathbf{u}^i + \Delta t \left(\frac{1}{2} (D_u \mathbf{u}^i + D_u \tilde{\mathbf{u}}^{i+1}) + F^i \right) \\ \tilde{\mathbf{w}}^{i+1} &= \mathbf{w}^i + \Delta t \left(\frac{1}{2} (D_w \mathbf{w}^i + D_w \tilde{\mathbf{w}}^{i+1}) + G^i \right) \end{aligned} \quad (3.20)$$

This is then rearranged in term of the intermediate approximations so only known terms exist on the right hand side:

$$\begin{aligned} \tilde{\mathbf{u}}^{i+1} &= K_u^{-1} [M_u \mathbf{u}^i + \Delta t F^i] \\ \tilde{\mathbf{w}}^{i+1} &= K_w^{-1} [M_w \mathbf{w}^i + \Delta t G^i] \end{aligned} \quad (3.21)$$

The matrices are linear combinations of the previously defined D_u, D_w .

$$\begin{aligned} M_u &= \left[I + \frac{\Delta t}{2} D_u \right], & M_w &= \left[I + \frac{\Delta t}{2} D_w \right] \\ K_u &= \left[I - \frac{\Delta t}{2} D_u \right], & K_w &= \left[I - \frac{\Delta t}{2} D_w \right] \end{aligned}$$

The non-linear functions at the next timestep can therefore be approximated using these intermediate solutions.

$$\begin{aligned} \tilde{\mathbf{F}}^{i+1} &= \mathbf{F}(\tilde{\mathbf{u}}^{i+1}, \tilde{\mathbf{w}}^{i+1}) \\ \tilde{\mathbf{G}}^{i+1} &= \mathbf{G}(\tilde{\mathbf{u}}^{i+1}, \tilde{\mathbf{w}}^{i+1}) \end{aligned}$$

The approximations for the implicit non-linear terms will be substituted into the full Crank-Nicolson scheme, equations (3.19.)

$$\begin{aligned} \mathbf{u}^{i+1} &= \mathbf{u}^i + \frac{\Delta t}{2} \left(D_u \mathbf{u}^i + D_u \mathbf{u}^{i+1} + \mathbf{F}^i + \tilde{\mathbf{F}}^{i+1} \right) \\ \mathbf{w}^{i+1} &= \mathbf{w}^i + \frac{\Delta t}{2} \left(D_w \mathbf{w}^i + D_w \mathbf{w}^{i+1} + \mathbf{G}^i + \tilde{\mathbf{G}}^{i+1} \right) \end{aligned} \quad (3.22)$$

This system will finally be rearranged so we have a forward stepping process with all the known values on the right.

$$\begin{aligned} \mathbf{u}^{i+1} &= K_u^{-1} [M_u \mathbf{u}^i + \frac{\Delta t}{2} (\mathbf{F}^i + \tilde{\mathbf{F}}^{i+1})] \\ \mathbf{w}^{i+1} &= K_w^{-1} [M_w \mathbf{w}^i + \frac{\Delta t}{2} (\mathbf{G}^i + \tilde{\mathbf{G}}^{i+1})] \end{aligned} \quad (3.23)$$

The entire numerical scheme requires multiple steps from defining the initial matrices, approximating the intermediate values and finally integrating the entire process over time (Equation 3.23). The matrices are relatively easy to decompose and subsequently invert as they only have have terms on the leading diagonal, subdiagonal, superdiagonal and antidiagonal.

3.4 Numerical accuracy

The Crank-Nicolson is an order two accurate numerical scheme with respect to both the space and time for the heat equation. The method is however of order one spatial accuracy for the second equation of the model due to the advection term. The error should be of order two accuracy with respect to the timestep. It is unclear if the error will be order one or two accurate with respect to the spatial step, the less desirable being the former.

Timestep size

The error with respect to the timestep size will be examined first. A sufficiently large spatial step of $\Delta x = 1$ is chosen to ensure that the solution remains stable as the timestep size increases. The total error of the solution will be a function of the timestep size.

$$\epsilon(\Delta t) = \frac{1}{N} \sum_{j=1}^N \sqrt{(u_j^M - u(T, x_j))^2} \quad (3.24)$$

The numerical simulation will be run with different grid resolutions in order to compute the order of accuracy. The parameters will be set $\ell = 100, a = 2.2, b = 0.45, \nu = 182.5$. Random initial perturbations from the vegetative steady state will be taken at each grid point (This will be formally stated in the next chapter). The random seed will be fixed for each simulation using the `rng` command and iterated over $t \in [0, 100]$.

The true solution will be approximated to be the numerical simulation with the smallest relative timestep, $\Delta t = 2 \times 10^{-4}$. The error for each simulation will be taken with respect to this empirical *true* solution.

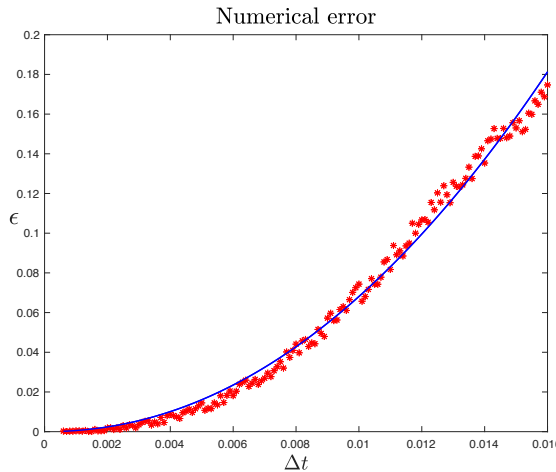


Figure 3.1: $\ell = 100, a = 2.2, b = 0.45, \nu = 182.5$. The timesteps are evaluated at $\Delta t = [5 \times 10^{-4}, 1.6 \times 10^{-4}]$ of 10^{-4} increments.

The error of the solution grows at a non-linear rate with respect to the timestep size. The numerical error will be fitted to function $\epsilon(\Delta t) = q\Delta t^p$ using the method of least squares. This fits the optimum function parameters by minimising the sum of the square residuals.

$$S = \sum_{i=1}^n \epsilon(\Delta t_i)^2 \quad (3.25)$$

This was implemented in MATLAB using the `lsqcurvefit` function. The value of the fitted index $p = 2.08$, supporting that the numerical method is order two accurate with respect to the timestep size.

Spatial step size

It is more difficult to calculate the error for different spatial steps as the solution must be defined on grids of different resolution. The parameters of the model will be set the same as the previous section. The timestep will be fixed to the following: $\Delta t = 10^{-2}$.

The error will depend on the spatial step size for each simulation:

$$\epsilon(\Delta x) = \frac{1}{N} \sum_{j=1}^N \sqrt{(u_j^M - u(T, x_j))^2} \quad (3.26)$$

The true empirical solution will be the simulation for $\Delta x = 0.1$. The simulation will be run over the following set $R_x = [\Delta x_1, \dots, \Delta x_c]$, $\Delta x_1 = 0.01$, $\Delta x_c = 1.0$ and $|R_x| = 100$. The spatial error will be calculated for each simulation at the final timestep defined at $T = 50$.

Working out the total error is not a trivial task as the spatial domain is mapped over a different number of grid points for each iterate. In order to calculate the difference the resolution must be adjusted to that of the most coarse grid, for $\Delta x = 1$ in this case. The error can then be calculated from the two vectors of equal size. The initial conditions must be kept fixed for each simulation and therefore a cosine wave will be used as the initial perturbation $u(x, 0) = u_1 + 0.002 \times \cos(\frac{2\pi \cdot 5}{100}x)$. This wavenumber has a positive growth rate: $k_5 \in K_+(2.2, 100)$, $\text{Re}\lambda(k) > 0$.

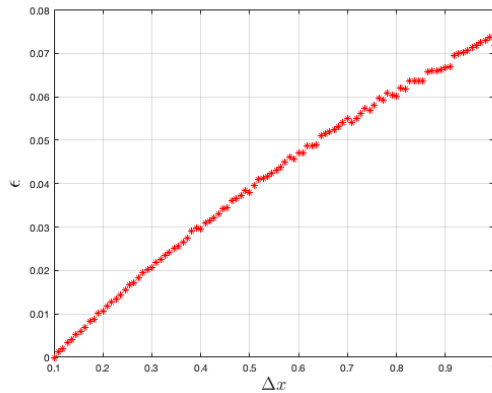


Figure 3.2: $\ell = 100$, $a = 2.2$, $b = 0.45$, $\nu = 182.5$. $\Delta t = 0.01$. The gridpoints are evaluated at $\Delta x = [0.1, 1]$ over 9×10^{-3} increments

The model is order one accurate with respect to the spatial step size. The error of the numerical solution will be given by the following:

$$\epsilon = O(\Delta x) + O(\Delta t^2) \quad (3.27)$$

For the majority of simulations a spatial step size of $\Delta x = 1$ and a time step size $\Delta t = 5 \times 10^{-3}$ was chosen. This will be adjusted if more accurate simulations are required for the analysis. This is a payoff between numerical accuracy and the time taken for the simulation to run. The time taken for the simulation to finish is proportional to the inverse of the time step and approaches infinity as $\Delta t \rightarrow 0$.

Chapter 4

PDE simulation observations

This previous chapter defined the steps to numerical simulate the partial differential model. This chapter explores the development and behaviour of the spatial patterns.

Chapter 3 studied the linear stability of the Klausmeier model and that diffusion-driven instability will form spatial patterns of particular frequency depending on the sign of the dispersion relation $\lambda(k)$. The advection of water downhill will force this eigenvalue to be of complex form (See equation 2.26) resulting in the uphill migration or the bands and the formation of a stable travelling wave (Klausmeier 1999; J.A Sherratt 2013). The growth of the non-uniform perturbations will be restricted by the non-linear terms of the model eventually forming a spatially stable solution (Murray 2003).

The Klausmeier model assumes that the vegetation exist on a sloped domain in which the gradient is defined by the parameter ν . The speed c will be empirically calculated from the model as the distance travelled over an arbitrary length of time $t = 1$. This mechanism will explain the Tiger bush phenomenon, see the literature review for more in depth analysis.

The frequency of the solution must be distinguished from the wavenumber. Perturbations of a particular wavenumber, see equation 2.13, will grow over time and the frequency will refer to the final stable travelling wave. The frequency will also be restricted to a factor of the domain length.

Suppose that the eventual stable pattern exists $\forall t > T$ then the solution can be expressed as a travelling wave $u(x, t) = U(x - ct)$ (J.A Sherratt 2013). This fixed in time will be expressed as a Fourier series (Weisstein 2022).

$$U(x) = a_0 + \sum_{j=1}^{\infty} a_j \cos\left(\frac{2\pi j x}{\ell}\right) + \sum_{j=1}^{\infty} b_j \sin\left(\frac{2\pi j x}{\ell}\right) \quad (4.1)$$

The solution is a combination of sinusoidal functions with frequency restricted by the domain length. The spatial frequency (ξ) of the fixed wave will be the unit cycles of $U(x)$ over unit distance which should correspond to some wavenumber $k \in \mathbb{K}(\ell)$.

$$\xi = \frac{1}{\gamma} \quad (4.2)$$

4.1 Initialising the simulation

Before running the numerical simulation then certain parameters must be fixed. Firstly the domain size will be set; throughout this project a domain of $\ell = 100$ will be taken. The parameter triplet (a, b, ν) will be then chosen and the appropriate vegetative steady state (u_1, w_1) calculated.

The base parameters will be set $(a, b, \nu) = (2.2, 0.45, 182.5)$. The vegetative steady state will be perturbed from steady state at each grid point of the discretised domain. Two different types of perturbations will be examined; randomly generated and a combination of cosine waves. There will be a base line for the distinction of a stable travelling wave; the amplitude of the final wave must be

greater than the initial perturbation take. The hostile conditions would not sustain homogeneous coverage of vegetation close to the tipping point which was understood early on (White 1970).

4.2 Random initial conditions

Random initial condition consider that a small random perturbation is added to each grid point. The initial system has uniform distribution of vegetation with small perturbations at each point, the system is close to the tipping point and so this spatially homogeneous spread is not sustainable and hence patterns will emerge. The vector \mathbf{u} at the first time step will be taken as the following:

$$\mathbf{u}^1 = u_1(\mathbf{J} + \alpha\boldsymbol{\mu}) \quad (4.3)$$

The vector $\boldsymbol{\mu} = [\mu_1, \mu_2, \dots, \mu_N]^t$ is a multivariate random vector taken from the random uniform distribution $\mu_i \in U[0, 1]$ which is then scaled by $\alpha = 0.02$. The multivariate random variable can be reused for simulations by fixing the random seed via the `rng` command. The vector \mathbf{J} is an $N \times 1$ column vector containing one. The initial condition is simply noise centred at the equilibrium point forming disordered levels of vegetative density over space and with no defined spatial frequency. This method will not favour any particular initial frequency. Random noise is consistent in all biology system and as Turing-instability is sensitive to small perturbations certain certain wave modes will exponentially grow over time (Maini et al. 2012).

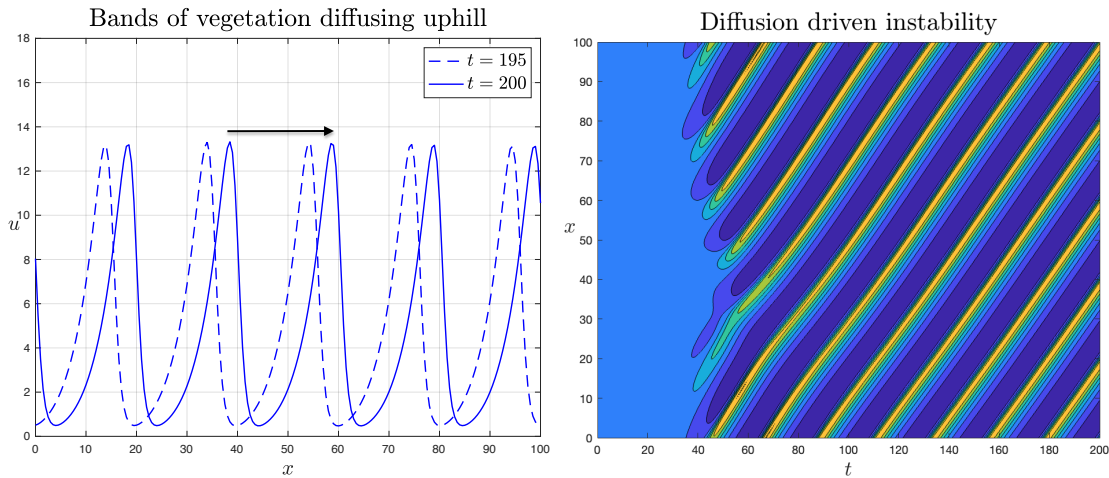


Figure 4.1: $a = 2.2, b = 0.45, \nu = 182.5, \Delta x = 1, \Delta t = 5 \times 10^{-3}$. Simulated over a total time $t \in [0, 200]$ The right is the contour plot over the spatiotemporal domain

The contour plot maps the development of the vegetative bands over time from the random initial conditions. The random noise smooths over time over an initial transient period. The solution spatially arranges itself into a regular pattern of growing amplitude before finally forming a fixed travelling wave. The pattern moves diagonally over time corresponding to uphill migration of spatial period $\gamma = 20$. For this simulation the frequency of stable solution is $\xi = k_5 = \frac{2\pi \cdot 5}{100}$, the wavenumber of the highest growth rate (see figure 2.1). The eventual pattern which forms will depend on the initial arrangement of the vegetative perturbations. To understand the general evolution of the travelling wave the model will be simulated 2000 times with different random initial perturbations. The resulting frequency of the stable solution is calculated and assigned a relevant $k_j \in \mathbb{K}(\ell)$.

j	k	Occurrence (%)
4	0.251	18.65
5	0.314	75.10
6	0.377	6.25

The eventual solution frequency corresponds to the wavenumber of the top three highest growth rates, supporting the dispersion relation in figure 2.1. The five-wave pattern has the highest respective growth rate making up the largest proportion (75.1%) of simulations.

4.3 Frequency analysis

Random initial conditions smooth and rearrange to form distinct patterns. The initial conditions remove any biased tendency for the solution to develop a particular frequency. The travelling solution is a trigonometric summation of different frequencies. The prevalence of each frequency in the solution can be tracked over time from sinusoidal initial conditions.

For $(a, b, \nu) = (2.2, 0.45, 182.5)$ and $\ell = 100$ then the set of wavenumbers which will grow over time (See Figure 2.4) is given by the following set:

$$\mathbb{K}_+(2.2, 100) = \left\{ \frac{2\pi j}{100} : j \in [2, 10] \subset \mathbb{N} \right\} \subset \mathbb{K}(\ell)$$

As $|\mathbb{K}_+| = 9$ then only a handful of wave frequencies will be tracked. The initial conditions will be the sum of these waves. There is also an offsetting parameter included, $\beta_j \in U[0, 100]$ (rounded to the nearest integer) to randomise the location of the waves.

$$u(x, 0) = u_1 + 0.05u_1 \cdot \frac{1}{|\mathbb{K}_+|} \sum_{j=2}^{10} \cos(k_j(x - \beta_j)) \quad (4.4)$$

The frequency domain of the solution will be gathered using the Fast Fourier Transform (FFT) algorithm. The FFT function will retrieve the frequency components of the solution with data sampled at each spatial step. The initial condition of the numerical simulation will be given by:

$$\begin{aligned} \mathbf{u}^1 &= u_1(\mathbf{J} + \alpha \mathbf{Q}) \\ Q_i &= \frac{1}{|\mathbb{K}_+|} \sum_{j=2}^{10} \cos(k_j(x_i - \beta_j)) \end{aligned} \quad (4.5)$$

The vector \mathbf{Q} contains the sum of the sinusoidal elements for $\forall k_j \in \mathbb{K}_+$. At each grid point x_i (for $i \in [1, N]$ see indexing 3.1).

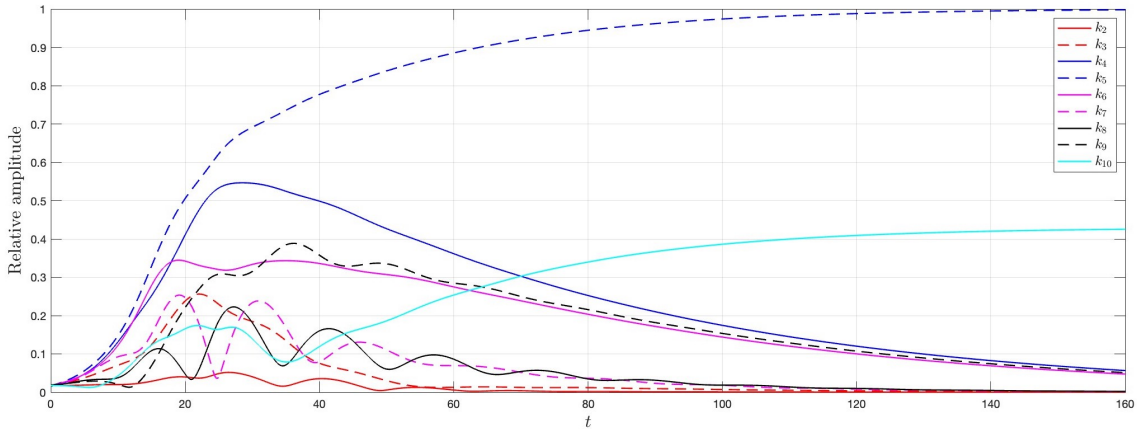


Figure 4.2: $a = 2.2, b = 0.45, \nu = 182.5, \ell = 100$. The evolution of particular frequencies over time. The simulation used $\Delta x = 0.5, \Delta t = 0.005$ over a total length $T = 200$

The frequency plot (Figure 4.2) shows there is initial transient behaviour followed by two spatial frequencies dominating the solution. The primary frequency of the solution is k_5 followed by the k_{10} (The multiple of the primary wave frequency). Note there are also FFT peaks at k_{15}, k_{20}, k_{25}

(frequencies a factor of k_5) in diminishing amplitudes. These wavenumbers do not have a positive growth rate according to the linear analysis however the common factor k_5 does.

Initially the frequencies $\xi = k_4, k_5, k_6$ all grow at the greatest rate which is consistent with the linear analysis. However at a certain point these frequencies peak and then slowly diminish to a relative amplitude of zero. The frequencies ($\xi = k_7, k_8$) initially oscillate in relative prevalence before diminishing to zero. The travelling wave solution $U(x)$ (fixed in time) is comprised of the primary frequency $\xi = k_5$ and the harmonic factors in reducing amplitude.

The system will behave differently for a higher level of rainfall; the steady state has a higher density of vegetation and is potentially more robust to diffusion driven instability. From the linear analysis the range of possible wavenumbers narrows with the solution favouring a higher spatial frequency (see Figure 2.6). The level of rainfall will be chosen to be $A = 3.1$ which is close to the Turing-Hopf point. The range of wavenumbers of positive growth are given by:

$$\mathbb{K}_+(3.1, 100) = \left\{ \frac{2\pi j}{100} : j \in [5, 8] \subset \mathbb{N} \right\}$$

Similar to previously the initial conditions will be set:

$$u(x, 0) = u_1 + 0.05u_1 \cdot \frac{1}{|\mathbb{K}_+|} \sum_{i=5}^8 \cos(k_j(x - \beta_j)) \quad (4.6)$$

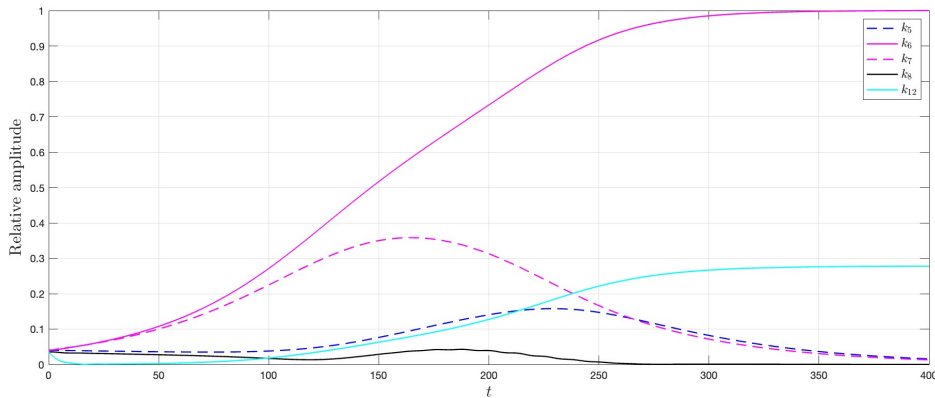


Figure 4.3: $a = 3.1, b = 0.45, \nu = 182.5, \ell = 100$. The evolution of particular frequencies over time. The simulation used $\Delta x = 0.5, \Delta t = 0.005$ over a total length $T = 400$

The formation of the stable patterns takes a longer time to occur; eventually settling at $T = 300$ rather than $T = 120$ for the previous case. The dominating frequency of the solution is $\xi = k_6$ with the harmonic k_{12} existing at 0.28 the relative amplitude. The dispersion relation $\lambda(k)$, see figure 4.4, explains the slow growth of the particular frequencies.

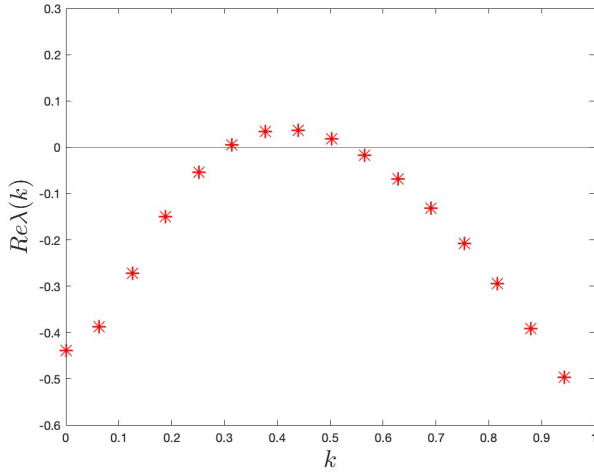


Figure 4.4: $a = 3.1, b = 0.45, \nu = 182.5$. The dispersion relation $\lambda(k)$ over the domain size $\ell = 100$.

For low levels of rainfall the equilibrium is far more sensitive to perturbations and will form patterns at an accelerated rate. This is understood by looking at the dominant eigenvalue for each frequency of a positive growth rate.

$$\mathbb{K}_+(1.0, 100) = \left\{ \frac{2\pi j}{100} : j \in [1, 10] \subset \mathbb{N} \right\}$$

The *y-axis* scale had to be raised (compared to figure 4.4) to capture the high growth rates of each wavenumber for this lower level of rainfall.

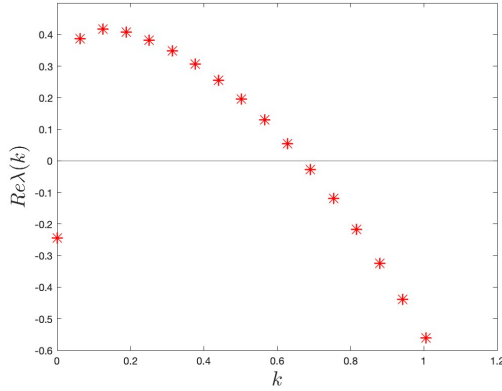


Figure 4.5: $a = 1.0, b = 0.45, \nu = 182.5$. The dispersion relation $\lambda(k)$ over the domain size $\ell = 100$.

The wavenumber peaks at a lower value demonstrating the systems inclination to form waves of a lower spatial frequency. The prevalence of each frequency from the sinusoidal perturbation can be examined over time.

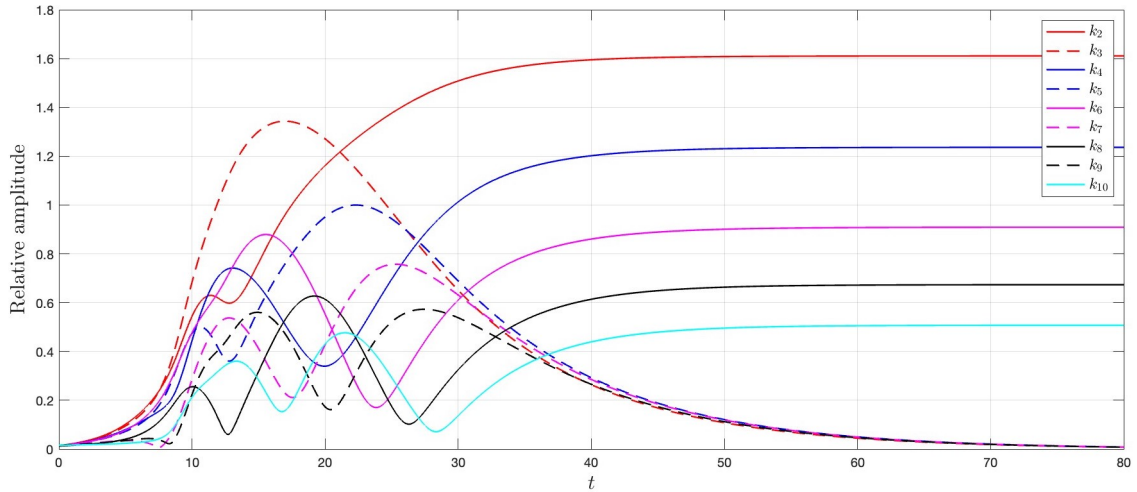


Figure 4.6: $a = 3.1, b = 0.45, \nu = 182.5$. The evolution of particular frequencies over time. The simulation used $\Delta x = 0.5, \Delta t = 0.005$ over a total length $T = 80$

The stable pattern forms fastest for the lower rainfall level. The frequency of the resulting solution takes $\xi = k_2$. The existence of underlying harmonic frequencies in the final solution is more clear in this case as the wavenumbers of even indexing all appear in the final solution. Interestingly the k_3 frequency initially dominates the solution before tending to zero resulting in the frequency of k_2 to prevail. The vegetative steady state is more sensitive to spatial perturbations given closer proximity to the limit point $a = 2b$.

As the rainfall levels decrease the spatial period of the bands reduce which ties in with observations of tiger bush; the phenomenon this model aims to replicate. The observation seen in (White 1970; Valentin, d'Herbes, and Poesen 1999) demonstrate that bands are located further apart for lower levels of rainfall.

4.3.1 Final frequency

Given a combination of initial frequencies then certain wavenumbers will dominate the solution over time. The system may develop different spatial frequencies given that only one wavenumber is present in the initial condition. Setting $(a, b, \nu) = (2.2, 0.45, 182.5)$ and an increased domain size $\ell = 256$ to ensure a higher clarity of eigenvalues.

$$\mathbb{K}_+(2.2, 256) = \left\{ \frac{2\pi j}{256} : j \in [5, 26] \right\} \quad (4.7)$$

The model is simulated with initial conditions $u_0 + 0.02 \cos(k_j x)$ and the final frequency (ξ) of the solution recorded.

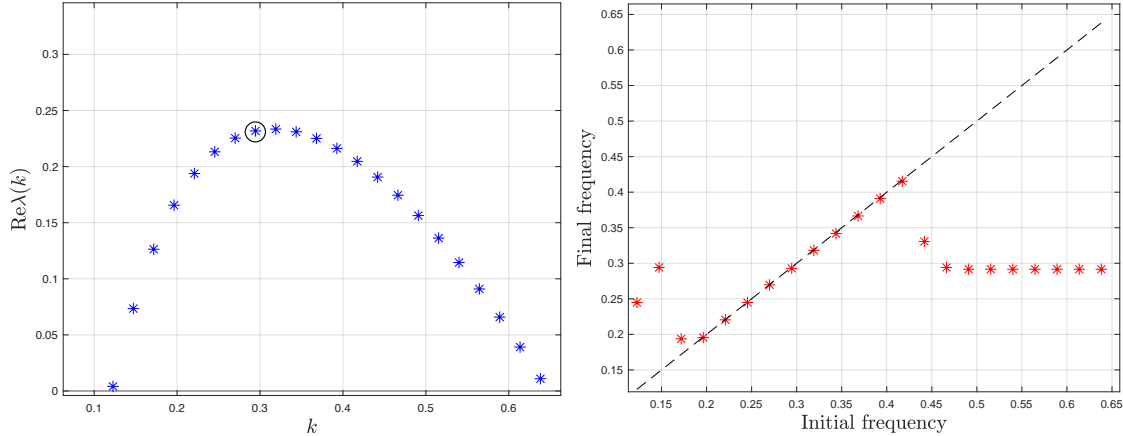


Figure 4.7: $a = 2.2, b = 0.45, \nu = 182.5, \ell = 256$. The left figure is the growth rate for each possible wavenumber of a positive eigenvalue value. The right plots the resulting wavenumber frequency of the final solution given the respective initial conditions.

The central wavenumbers $k_j \in [k_8, k_{17}]$ retains the initial frequency existing on the $y = x$ line. For initial conditions of extreme frequencies then the solution will tend to a pattern of the higher growth rates. This is seen for $k_j \in [k_{19}, k_{26}]$ which despite having high initial frequencies all settle to k_{13} . This may suggest that higher frequencies are less stable and able to migrate to a lower frequency more readily.

4.3.2 Bottleneck frequency

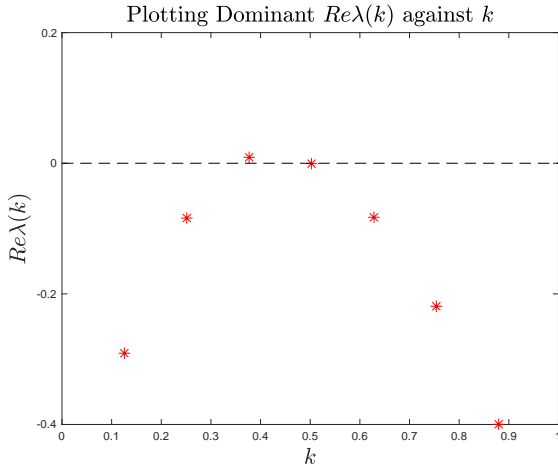
The dispersion relation $\lambda(k)$ depends on the vegetative steady state and importantly the level of rainfall. For $A = 2.2$ a relatively high number of allowable wavenumbers (see figure 2.1) have positive growth rate. As rainfall increases the range of allowable wavenumbers of positive growth rate reduces (See figure 2.5) up until the Turing-Hopf bifurcation.

The bottleneck frequency will define a set of parameters and domain length such that $|\mathbb{K}_+(a, \ell)| = 1$. The resulting stable state solution should have frequency $\xi = k_j$ for $\mathbb{K}_+(A, \ell) = \{k_j\}$.

Using trial and error then the following parameters $(3.2, 0.45, 182.5)$ with respective domain size $\ell = 50$ hosts only one wavenumber of positive growth rate. The domain size is smaller than previously used so the set of wavenumbers will be more sparsely spread. Note that there will still be other harmonic frequencies prevalent in the solution.

$$\mathbb{K}(50) = \left\{ \frac{2\pi j}{50} : j \in \mathbb{N} \cup 0 \right\} \quad (4.8)$$

Its important to be specific when labelling this set.

Figure 4.8: $\ell = 50, a = 3.2, b = 0.45, \nu = 182.5$.

The only wavenumber which has a positive growth rate is $k_3 = \frac{2\pi}{50}$. The model is simulated 1000 times with initial random noise added to the vegetative equilibrium of magnitude $\alpha = 0.02$. The wavelength γ of the solution is calculated at the final time step after running for $t \in [0, 400]$ and frequency $\xi = \frac{2\pi}{\gamma}$. The simulation was run for a relatively long time period to ensure that a stable travelling wave forms. Only 6.3% of resulted in pattern formation however in each case $\xi = k_3$. The dominant frequency of the solution is the only wavenumber of positive growth rate.

It's important to observe that only a very small proportion of simulations actually resulted in vegetative patterns forming demonstrating the significance of the initial conditions. Certain conditions will favour the correct frequency simply due to random arrangement.

4.4 Wave speed analysis

The vegetative stripes migrate uphill, albeit extremely slowly (Valentin, d'Herbes, and Poesen 1999). As the dispersion relation, $\lambda(k)$, is complex then the solution should diffuse uphill at speed $\text{im}\lambda(k)$, see equation 2.26.

For parameters (a, b, ν) and certain initial condition a travelling wave will form of a particular wave frequency; For $\forall t > T, u(x, t) = U(x - ct)$ modulo the domain length. The parameter c is the wavespeed of the solution and not is explicit to the model. The wavespeed of the solution can be calculated from the numerical simulation and compared for different rainfall values. The wavespeed will be the distance travelled over the spatial domain over a single unit of time. In order to have a high accuracy estimate the spatial domain must have a high resolution $\Delta x = 0.2, \Delta t = 0.005$. Once a steady travelling wave solution forms then the median distance travelled over $t = 5$ will be calculated over time.

In order to fix variables the speed of the wave will be taken to be a frequency of k_5 , $\ell = 100$ hence setting the initial condition $u(x, 0) = u_0 + 0.05 \cos(k_5 x)$. This particular frequency was chosen as $k_5 \in \mathbb{K}_+(a, 100)$ for a large parameter range.

a	c
1.6	2.4
1.8	2.8
2.0	3.2
2.2	3.6
2.4	4.4
2.6	4.8

There is a linear relationship between the level of rainfall and the speed that the wave travels over

the domain. Higher levels of rainfall will increase the rate that plants migrate uphill. Limited literature supports this as measuring the speed of bands takes decades and the level of rainfall of an area is variable over the years.

4.5 Frequency growth rate

The growth rate of the numerical solution for each particular wavenumber k should be consistent with the analytically determined $\lambda(k)$. The same initial condition format (see conditions 4.5) except with $\alpha = 0.0002$. The smaller the perturbation the more strongly it will support the linear analysis.

The model solution for a small perturbation is of the following form:

$$\begin{pmatrix} \hat{u}(x, t) \\ \hat{w}(x, t) \end{pmatrix} = \begin{pmatrix} \bar{u} \\ \bar{w} \end{pmatrix} e^{\lambda(k)t + ikx}$$

The amplitude of each frequency should grow over time proportionally to $\exp(\text{Re}\lambda(k)t)$. Using Fast Fourier transform each frequency of the solution can be extracted and analysed separately to calculate the unique growth rate. The simulation was run over $t \in [0, 10]$, before the non-linear terms will theoretically take effect and inhibit the growth.

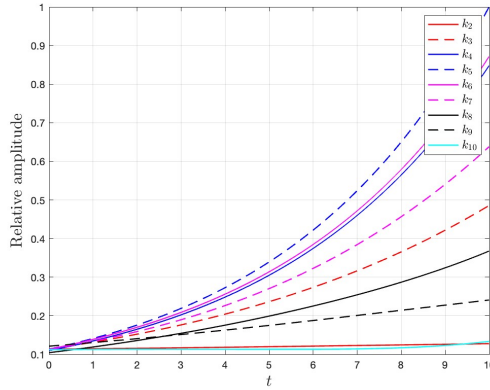


Figure 4.9: $a = 2.2, b = 0.45, \nu = 182.5$. The initial growth rates of each frequency of the initial perturbation. The simulation used $\Delta x = 0.5, \Delta t = 0.005$

Note that the growth rates of Figure 4.9 are normalised with respect to the maximum value (however this should not affect the calculation of the growth rate factor). Letting the vector \mathbf{m}_k contain the relative amplitude at each timestep i ; using the method of least squares it will be fitted to the function $f(t) = qe^{pt}$ using *lsqcurvefit* on MATLAB. The function acts to minimise the following sum by choosing the values q, p :

$$S = \sum_{i=1}^M [\mathbf{m}_k^i - f(\mathbf{m}_k^i)]^2$$

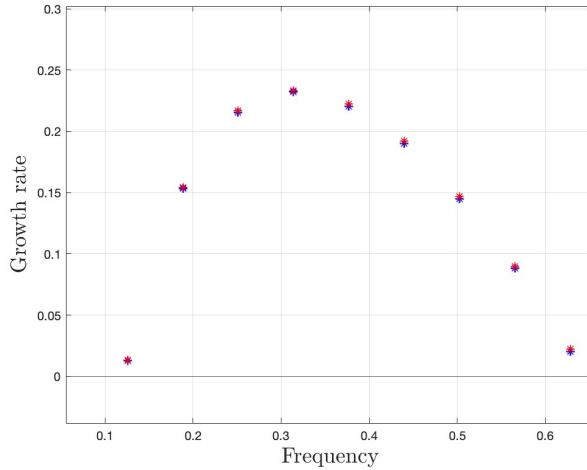


Figure 4.10: $a = 2.2, b = 0.45, \nu = 182.5$. The blue crosses are the numerically calculated growth rate. The red crosses are the plotted $\text{Re}\lambda(k)$ for each wavenumber. For the simulation $\Delta t = 10^{-3}, \Delta x = 5 \times 10^{-2}, \alpha = 2 \times 10^{-4}$

The numerical model clearly supports the linear analysis as the numerically calculated growth rates perfectly overlay the real part of the corresponding dominant eigenvalue. This observation is also consistent with different levels of rainfall.

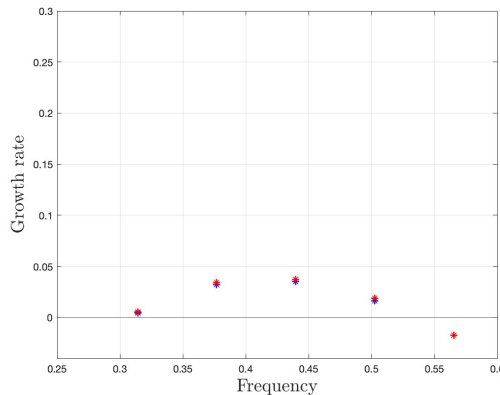


Figure 4.11: $a = 3.1, b = 0.45, \nu = 182.5$. The blue crosses are the numerically calculated growth rate. The red crosses are the plotted $\text{Re}\lambda(k)$ for each wavenumber. For the simulation $\Delta t = 10^{-3}, \Delta x = 5 \times 10^{-2}, \alpha = 2 \times 10^{-4}$

4.6 The wavelength of the solution

The wavelength of the bands will depend on the environmental condition and terrain of the ecosystem (Valentin, d'Herbes, and Poesen 1999). All factors will remain fixed except the level of rainfall.

Spatial patterns form given that $a \in (0.90, 3.28)$, the tipping point and the Turing-Hopf bifurcation. As seen in the linear analysis the dominant wavenumber increases with rainfall, see figure 2.5 (Corresponding to shorter wavelength). It would be expected that the numerical solutions shadow this.

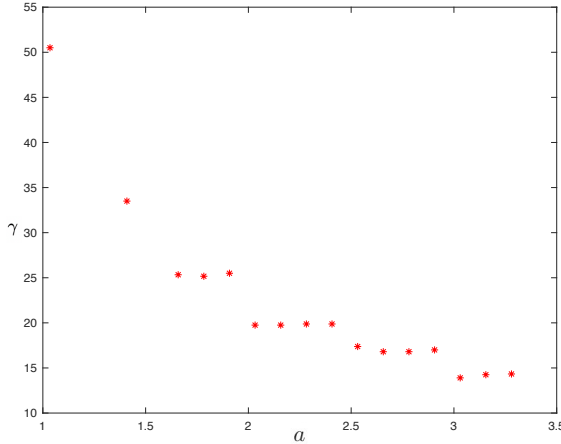


Figure 4.12: $\ell = 100, b = 0.45, \nu = 182.5$. The simulation used random initial conditions with $\Delta x = 1, \Delta t = 0.01, T = 500$. The median length has been plotted over 10 simulations

Taking random initial conditions the model was simulated at regular intervals between $a \in [1, 3]$. The median wavelength of the solution was taken for 10 simulations for each rainfall value in order to make a better estimate. The distance between bands increase as rainfall decreases, the wavelengths must be a factor of ℓ .

4.7 Conclusions

The system is more sensitive to perturbations when the conditions are closer to the tipping point. This is seen in the frequency analysis in which the stable solution develops at a much faster rate for lower levels of rainfall. Spatial patterns will form more readily in hostile conditions which is supported by the linear analysis of the dispersion relation and the numerical simulations. The numerical growth rates are highly consistent with analytically calculated dispersion relation.

As seen in Figure 4.12, the period of the wave will decrease with a higher level of rainfall. This corresponds to field results of the Tiger bush formation, see Figure 1.3 (Valentin, d'Herbes, and Poesen 1999), which shows that the stripes become more and more disperse with decreasing levels of rainfall. This was stated originally by Klausmeier, stating that as rainfall decreases then there will be *stripes of increasing wavelength, to no vegetation* (See figure 1.4).

The numerical simulations show that diffusion-driven instability will occur between the tipping point and Turing-Hopf bifurcation. This closely resembles the diagram (Figure 1.6) for the extended partial differential equation (Rietkerk, Dekker, et al. 2004). The Rietkerk model shows the increasing sparsity of vegetation as the resources are limited.

A major drawback of the model is not being able to see the relative length of each spatial band. The length of the band should decrease with the level of rainfall forming a more *Dashed pattern*, (See Figure 1.3). The model assumes that the surface water is immediately absorbed by the plant and does not model the diffusion of soil moisture. This was acknowledged by Klausmeier with the Rietkerk model (See equations 1.4) extended the system to both surface and soil water components.

Chapter 5

Existence of travelling waves

The Klausmeier partial differential model captures the uphill migration of steady waves. This is based off the water redistribution hypothesis, running downhill before being absorbed by the pioneering front of the band. Uphill migration takes place over decades and hard to experimentally observe (Valentin, d'Herbes, and Poesen 1999). The Rietkerk model (See equation 1.4) demonstrates that bands will also move uphill on sloped terrain. The Klausmeier equations model the Tiger bush phenomenon and not the more spotted style patterns seen on flat ground.

As previously seen the development of this solution depends on the initial conditions with a general tendency to adopt a frequency of the dominant growth rate. The advection of water is the core mechanism behind this slow uphill migration, the eigenvalue will be complex thus causing the solution to travel over space.

The solution can be written as a stable travelling wave of the following form:

$$\begin{aligned} u(x, t) &= U(x - ct) \\ w(x, t) &= W(x - ct) \end{aligned} \tag{5.1}$$

As seen before (Equation 2.14) the solution will be a fixed periodic function written as a Fourier series. The solutions travel with constant speed c , which depends on the imaginary part of the eigenvalue. The partial differential equation is defined on a finite domain of size ℓ and therefore $x - ct$ will be taken modulo the domain size. Taking $z = x - ct$ then using the chain rule the partial differential equations can be written with respect to the travelling wave solution (J.A Sherratt 2013). Note that the wave solution is a function of a single variable z and hence will be written as an ordinary differential equation:

$$\begin{aligned} \frac{\partial u}{\partial t} &= \frac{\partial U}{\partial z} \frac{\partial z}{\partial t} = -c \frac{dU}{dz} \\ \frac{\partial w}{\partial t} &= \frac{\partial W}{\partial z} \frac{\partial z}{\partial t} = -c \frac{dW}{dz} \\ \frac{\partial^2 u}{\partial x^2} &= \frac{d^2 U}{dz^2} \\ \frac{\partial w}{\partial x} &= \frac{dW}{dz} \end{aligned} \tag{5.2}$$

The partial differential model (Equations 2.2) can now be written in terms of the wave solutions $U(z), W(z)$:

$$\begin{aligned} \frac{dU}{dz} &= -\frac{1}{c} \left(WU^2 - bU + \frac{d^2 U}{dz^2} \right) \\ \frac{dW}{dz} &= \frac{1}{c + \nu} (WU^2 + W - a) \end{aligned} \tag{5.3}$$

To remove the second order derivative then a new variable V will be introduced such that $\frac{dU}{dz} = V$ forming the following system of ordinary differential equations:

$$\begin{aligned} U_z &= V \\ V_z &= -WU^2 + bU - cV \\ W_z &= \frac{1}{c+\nu} (WU^2 + W - a) \end{aligned} \tag{5.4}$$

These equations are difficult to comprehend as they depend on the variable $z = x - ct$. The equilibrium points of the partial differential system will also correspond to the steady states of this ordinary differential system. Bifurcation analysis of the wave equations will inform the parameter range that waves of particular lengths will exist, the speed of waves and demonstrate the locations in the parameter range in which the patterns are forced to change. This will also give a detailed understanding into the *Busse balloon* (Stelt et al. 2013; Rietkerk, Bastiaansen, Banerjee, Jvan de Koppel, et al. 2021) and the existence of waves beyond the tipping point.

The waves should persist beyond the tipping point, a pathway between the state of homogeneous vegetation and complete desert (Rietkerk, Bastiaansen, Banerjee, Jvan de Koppel, et al. 2021). The waves, once established, should be *self-perpetuating*, (White 1970).

5.1 Bifurcation analysis of the travelling wave solutions

The equilibrium points of the travelling wave solution will correspond to the equilibrium points of the spatially homogeneous partial differential equations. The wavespeed c is an input variable of the system offering the ability to adjust this parameter to analyse the behaviour. Numerical continuation will be used to understand the stability of the system and locate the bifurcation points.

The bifurcation points mark the transition of the stability of the ordinary differential system. Importantly the stability of the travelling wave system (ODE system) has no relevance to the stability of the Klausmeier model (PDE system). Previously a finite domain with periodic boundary conditions was implemented however for the ODE system no such notion exists and hence $\ell = \infty$; there are no limitations on the possible wavelength and frequency of the solution. This adds a new level of difficulty to draw comparisons to a fixed domain $\ell = 100$, the wavelength must be manually set in order to draw conclusion to the previous numerical analysis. The circular domain models a unit of the total theoretical area with periodic boundary conditions emulating an infinite region, a larger domain size may be more accurate in tracking the particular waves.

The parameters (a, b, ν) will be fixed and the wavespeed c altered in the first case. There will be a range $c \in (c_1, c_2)$ in which the resulting wave, $U(c)$, has a non-zero amplitude for an appropriate set of parameters. The points c_1, c_2 will be the respective supercritical and subcritical Hopf bifurcation points for the wavespeed parameter in which the system forms periodic orbits. The derivative $U_z(U, V, c) = 0$ is tracked close to the hyperbolic equilibrium with the relevant period and oscillatory limits calculated.

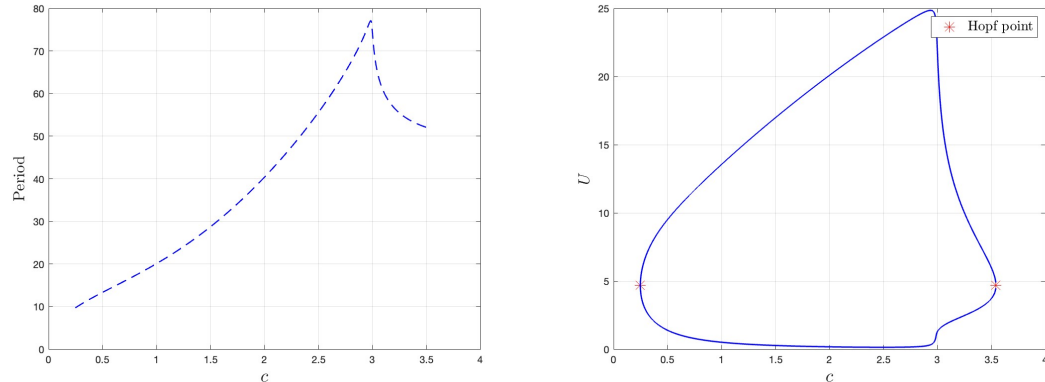


Figure 5.1: Bifurcation diagram with respect to wavespeed c , $a = 2.2$, $b = 0.45$, $\nu = 182.5$. The plot on the left tracks the speed that the wave travels against the period of the wave. The plot on the right plots the relative amplitude of the wave with the red stars marking the minimum and maximum speed of the waves.

The Hopf points are located at $c_1 = 0.248$ and $c_2 = 3.543$ which define the respectively fastest and slowest rate that a travelling wave can travel. The smallest possible period which exists is $\gamma = 10$ which travels at the slowest speed. This is interesting as $k_{10} \in \mathbb{K}_+(2.2, \ell)$ and the largest wavenumber in this set. The speed of the wave increases as the period increases (frequency decreases) until a period of $\gamma = 77$ which occurs at speed $c = 3$, the period quickly falls off after this point. The largest wavelength possible for the numerical simulation with $\ell = 100$ is 50 and hence the behaviour for higher periods will not be captured by the PDE simulation. This is a clear limitation of the partial differential numerical model as the wavelengths are restricted to a factor of the domain. The period and amplitude of the waves correspond to one another in which higher wavespeeds have a larger amplitude of oscillation.

The larger amplitude of oscillation signifies that the density of each band will increase as the period length increases. This is difficult to find comparable real world example however it shows that more biomass is contained in more sparsely spread stripes for the same ecological parameters.

5.1.1 Fixing the period

For Figure 5.1 the solution was numerically continued at the first Hopf bifurcation point to plot the relevant amplitude and period for periodic solutions. Using this data a particular point of period γ will be chosen to understand the range of existence as the rainfall parameter A is varied. Importantly in order to be consistent with a domain size $\ell = 100$ then periods of a wavelength factor were chosen; $\gamma \approx \frac{100}{3}, \frac{100}{4}, \frac{100}{5}, \frac{100}{6}$. Each wavelength exists over a subset of the A parameter range (A_1, A_2) forming a closed curve. The information will be contained in the following set for each wavelength:

$$\beta_\gamma = \{\{A, u_{min}, u_{max}\} : \forall A \in (A_1, A_2)\}$$

This will form a hereby named *Bubble region* for each wavelength which corresponds to the parameter range of existence and vegetative density.

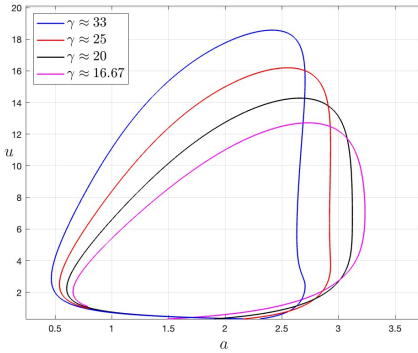


Figure 5.2: $b = 0.45, \nu = 182.5$. The parameter region in which waves of particular wavelengths will exist. the vertical length of each *bubble* are the limits of oscillation for each wave

The denominator of the wavelength corresponds to the number of waves within the domain and the travelling wave will be aptly named as such. The parameter range over which this particular wave exists is contained in the following table:

	# of waves	a_1	a_2	$(a_2 - a_1)$
3	0.47	2.70	2.23	
4	0.54	2.93	2.39	
5	0.60	3.12	2.52	
6	0.66	3.23	2.57	

Patterns of a greater number of waves exist over both a higher and broader parameter range. The amplitude of oscillation generally decreases with decreasing rainfall meaning reduced amount of biomass. This supports experimental evidence (White 1970)

Crucially every wave examined exists for values $a < 2b$ which is the theoretical cut-off point for vegetative steady states to exist (The tipping point). This is a significant observation as this demonstrates that vegetation in the form of a travelling wave will survive beyond this tipping point despite there being no technical vegetative steady state, waves exist in conditions which warrant a desert state. This supports the claim that spatial-organisation acts evade tipping points and a 'signal of resilience' Rietkerk, Bastiaansen, Banerjee, Koppel, et al. 2021. The patterns will exist within the Busse balloon as seen in Figure 1.7.

There are cross over points as a decreases in which the wave should switch from one wavelength to another. The PDE will be simulated at these cross over points to observe the behaviour of the wave and tact of collapse.

5.2 Critical transitions

The theory of critical transitions was explored in the literature review and signifies the instance in which a bistable system will switch to the opposing steady state (Scheffer et al. 2001a). There are two opposing stable steady states in this system. The natural formation of spatial patterns of increasing wavelength paves the way to a complete desert.

The transition of the three and four wave pattern over the finite $\ell = 100$ domain will be modelled. The three-wave pattern has spatial frequency $\xi = \frac{3\pi}{50}$, the four-wave pattern has spatial frequency $\xi = \frac{2\pi}{25}$. The wave pattern formed depends on the initial conditions, these are carefully chosen so the correct wave develops.

At this wave transition points then the solution of the desired frequency may never naturally develop from initial perturbations. In fact most of these transitions occur before the tipping point. To bypass this issue then a higher value of a will be simulated from to ensure that a stable solution

of the desired frequency develops. The rainfall is then reduced incrementally over time to monitor the wave collapse.

For the **three**-wave pattern the rainfall will be incrementally reduced over time from $t \in [0, 200]$, it will be written as the following function:

$$a(t) = 1.15 - (5 \times 10^{-3})t$$

For the **four**-peak wave the same technique was used here with an extended time period with an upper band $A = 1.4$, This will be simulated for $t \in [0, 300]$. The parameter a can again be written as a function of time for this case:

$$a(t) = 1.55 - (5 \times 10^{-3})t$$

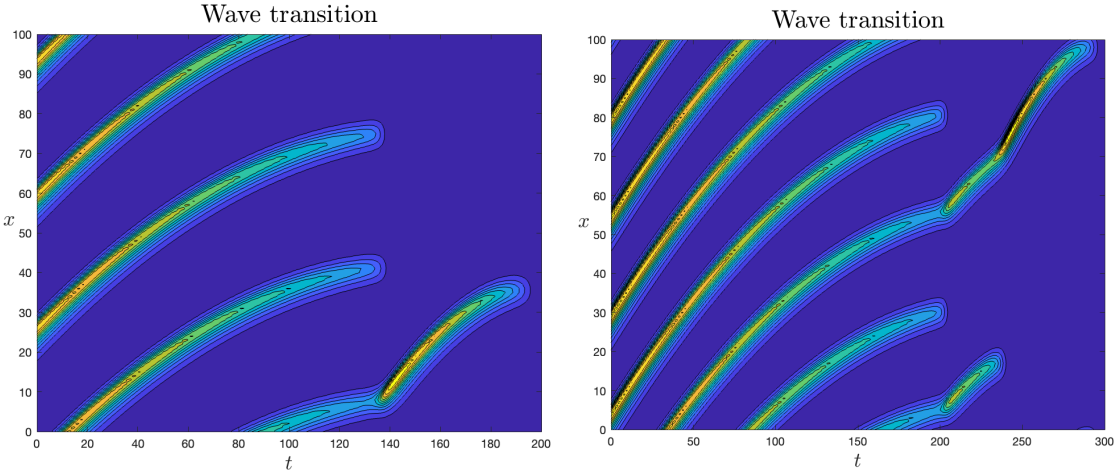


Figure 5.3: Wave transition with reducing levels of rainfall. The numerical simulation used $\Delta x = 1, \Delta t = 0.01, \ell = 100$. The left plot is the collapse of the three-wave spatial pattern. The right is the collapse of the four-wave pattern.

The pattern shifting behaviour will be determined to the nearest integer point in time as the exact transition is not entirely obvious. The three-wave pattern collapses to single wave at $t = 135$ which corresponds to $a = 0.46$. This supports the bifurcation analysis in which the lower limit for three-waves is at $a_1 = 0.47$. It would be expected that the single wave pattern exists for even lower values of A and the lowest boundary will define the final point in which vegetation is possible.

The four-wave pattern transitions to a single wave at $t = 205, a = 0.58$. This closely resembles the bifurcation analysis in which this lowest limit was at $a_1 = 0.54$. For both cases the patterns collapse to a single wave within the domain. As a is continually decreased the wave eventually ceases to exist occurring at $a = 0.22$ (to the nearest integer time value) in both cases. Using numerical continuation once again of the wave equations results in the following for the single wave pattern:

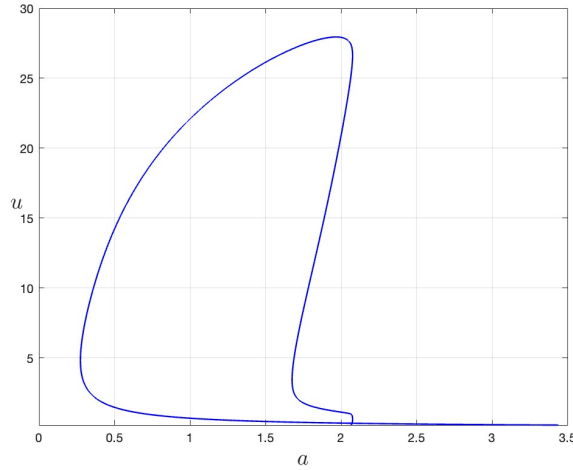


Figure 5.4: $b = 0.45, \nu = 182.5$. The existence of the single wave pattern over the rainfall parameter range.

The single travelling wave exists over $(0.28, 2.08)$. The numerical simulations suggest that the single-wave ceases at a lower level of rainfall however it is likely that this transition occurred gradually and therefore the value of a was overestimated. Over this domain size no spatial patterns exist lower than $a < 0.28$ which marks the absolute threshold for sustained vegetative existence.

The waves are unable to form given that $a < 2B$ however once stable patterns have formed then gradually reducing the rainfall parameter will result in vegetation existing much lower than anticipated in the form of travelling waves. The speed of the travelling wave will be a strong indication to predict the onset of a critical transition (Rietkerk, Bastiaansen, Banerjee, Jvan de Koppel, et al. 2021.)

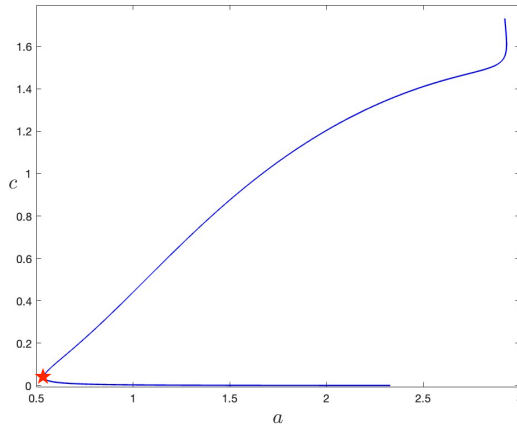


Figure 5.5: $b = 0.45, \nu = 182.5$. The wavespeed of the four-wave pattern over the spatial domain with a reducing level of rainfall

The speed of the wave decreases, Figure 5.2, with decreasing rainfall. The wave will continue to decrease in speed until the level of rainfall cannot sustain this pattern type. The red start marks the cusp point in which the travelling wave no longer exists. Note for each point there exists two solution for $a \in (0.54, 2.93)$; the solution of zero wavespeed will be the trivial non-pattern solution of zero amplitude. Vegetative bands travelling at a slower than previous speed may indicate that a critical transition will occur.

5.3 Conclusion

The simulations support the wave equation bifurcation analysis. The particular pattern only exists within the *Bubble region* with the wave collapsing as the rainfall is reduced beyond the limits of existence. The analysis supports the existence of the *Busse balloon* put forward by (Stelt et al. 2013; Rietkerk, Bastiaansen, Banerjee, Jvan de Koppel, et al. 2021) and shows that patterns will form given that the steady state is close to the tipping point (with rainfall lower than the Turing-Hopf bifurcation). For the spatially uniform system (See Figure 2.3) then given no spatial dispersion then the critical transition will occur given that the initial conditions are forced into the desert mode, the formation of vegetative patterns are a sign of resilience against this change. The patterns bridge the gap between uniform vegetative coverage and desert state and only exist in one direction over time, they cannot form with increasing levels of rainfall from an initial desert steady state. The banded organisation of the Tiger Bush will hint to the onset of a critical transition of the ecosystem. If the spatial periods of the bands increase over time then this will infer that the system is tending towards an eventual shift. The banded patterns exist kilometres across with grass migration speed estimated to be $0.3 - 1.5\text{m}/\text{yr}$ (Klausmeier 1999; Worral 2006), the process is on an extremely slow. Critical transitions may be difficult to predict as the patterns have only been observed over the past 80 years.

The Klausmeier model is effective for multiple reasons. Firstly the model is simplistic, each parameter has a clear biological meanings and can be easily adjusted. The mechanism is simple and justifies real-world observations; water flows downhill and vegetation diffuses over space with the non-linear term explaining the facilitative influence that plants have on the soils infiltration rate. The model provides a clear mechanism behind the intrinsic formation of vegetative patterns. Mathematical simulation show how the system responds to changes which would otherwise be extremely difficult to observe in the natural world, predict the onset of a critical transition and finally offer methods of human intervention to increase the resilience of a system.

Appendix A

Appendix Title

This contains the skeleton code I wrote to model the Klausmeier functions:

A.1 Functions

A.1.1 Locating equilibria

```
function [u_eq,w_eq] = find_equilibria(a,b,nu)
%finds the equilibria depending on a,b,nu. This assumes a>2b
x0 = [0 a];
x1 = [(a+sqrt(a^2-4*b^2))/(2*b), 2*b^2/(a+sqrt(a^2-4*b^2))]; %vegetative stable steady state
x2 = [(a-sqrt(a^2-4*b^2))/(2*b), 2*b^2/(a-sqrt(a^2-4*b^2))]; %Vegetative unstable steady state
u_eq = x1(1); %The u equilibrium for vegetative steady state
w_eq = x1(2); %the w equilibrium
end
```

A.1.2 Eigenvalues

This function works out the real part of maximum eigenvalue $\lambda(k)$ for a particular wavenumber input k . This works out $M_{eq}(k)$ as see in chapter 3 and the resulting dispersion relation.

```
function [max_real_eig,eigenvector] = eig_for_k(par,eq,k)

%THis function generates the max real eigenvalue and corresponding
%eigenvectors for the k input!
a = par(1);
b = par(2);
nu = par(3);
u0 = eq(1); %the equilibria are defined
w0 = eq(2);
fu = 2*w0*u0-b; %the partial derivatives defined at the equilibrium point
fw = u0^2;
gu = -2*w0*u0;
gw = -u0^2-1;

Ma = [fu-k^2, fw; gu,gw+1i*k*nu]; %this is the spatial jacobian matrix! Depends on wavenumber
max_real_eig = max(real(eigs(Ma))); %working out the real part of the max Eigenvalue
[Vv,d_lambda] = eigs(Ma);

if real(d_lambda(1,1)) > real(d_lambda(2,2))
    eigenvector = Vv(:,1);
else
    eigenvector = Vv(:,2);
```

```

end
%This chooses the eigenvector of the LARGEST eigenvalue! this is either in
%the 1st or 2nd position. Simply choosing the eigenvector which corresponds
%to the largest eigenvalue

end

```

A.1.3 Terms of the Crank-Nicolson method

```

function [MU,MW,KU_inv,KW_inv] = matrix_form(par,N,dx,dt)
%This function generates the necessary matrices used in the Crank-nicolson method.
%this outputs MU,MW,KU_inv,KW_inv!
a = par(1);
b = par(2);
nu = par(3);

Du = zeros(N,N); %setting up the Du matrix
Dw = zeros(N,N); %setting up the Dw matrix
BL = [1/(dx^2), 0; 0, 0]; %matrix with the corresponding spatial derivative
A_m = [-2/(dx^2) 0; 0, -nu/dx];
BR = [1/(dx^2), 0; 0, nu/dx];

%filling in the matriz Du, and Dw
for i=1:N-1
    Du(i,i) = A_m(1,1); %filling in the leading diagonal
    Du(i,i+1) = BR(1,1); %the subdiagonal
    Du(i+1,i) = BL(1,1); %the superdiagonal
end

Du(end,1) = BR(1,1); %finally the terms in the corners to ensure
% that the ends of the spatial domain are connected
Du(1,end) = BL(1,1);
Du(end,end) = A_m(1,1);

for i=1:N-1
    Dw(i,i) = A_m(2,2);
    Dw(i,i+1) = BR(2,2);
    Dw(i+1,i) = BL(2,2);
end
Dw(end,1) = BR(2,2);
Dw(1,end) = BL(2,2);
Dw(end,end) = A_m(2,2);

Id = eye(N); %N*N identity matrix
MU = Id+0.5*dt*Dw; %These are the matrices used in the Crank-Nicolson method
MW = Id+0.5*dt*Du;
KU = Id-0.5*dt*Dw;
KW = Id-0.5*dt*Du;
KU_inv = inv(KU); %The inverse of Ku and Kw
KW_inv = inv(KW);
end

```

A.1.4 The Crank-Nicolson method

```

function [U_next,W_next] = Crank_fun_revised(par,KU_inv,KW_inv,MU,MW,dt,U,W)
%this works out the next timestep for U and W

a = par(1);
b = par(2);

```

```
nu = par(3);

F = W.*U.^2-b*U; %the F function
G = a-W-W.*U.^2; %The G function
%This calculates the intermediates!

U_tild = KU_inv*(MU*U+dt*F);
W_tild = KW_inv*(MW*W+dt*G);
F_tild = W_tild.*U_tild.^2-b*U_tild;
G_tild = a-W_tild-W_tild.*U_tild.^2;

%The final vectors at the next timestep. This integrates to the next
%timestep from the previous conditions.
U_next = KU_inv*(MU*U+0.5*dt*(F+F_tild));
W_next = KW_inv*(MW*W+0.5*dt*(G+G_tild));

end
```

A.2 Main code

```
clear all
%%
par = [3.26,0.45,182.5]; %the parameters
a = par(1); %the rainfall parameter
b = par(2); %the evaporation
nu = par(3); %the Hill angle
L = 100; %the domain length
if a<=2*b
    disp('a must be larger than 2b for non-trivial stable equilibria!')
else
    [u1,w1] = find_equilibria(a,b,nu); %this here find the vegetative steady state
end
eq = [u1,w1]
% The eigenvalues for each wavenumber k

Integer_length = 20; %the length of the possible wavelengths
k = (0:Integer_length)*2*pi/L; %The possible eig values
eigs = zeros(length(k),1);
eigenvector = zeros(length(k),2);
for i=1:length(k)
    [m_eig,vector]=eig_for_k(par,eq,k(i)); %this then generates the real parts of the
    %maximum eigenvalues for each k value
    eigs(i) = m_eig; %the list of max eigenvalues
    eigenvector(i,:) = vector; %the list of eigenvectors for each eigenvalue
end
plot(k,eigs,'k*');
yline(0)
%% Numerical simulation

dt = 0.005; %timestep size
T = 100; %The total time
dx = 1; %The spatial step
X = 0:dx:L %The domain length. From 0-L
N = length(X); %The number of spatial steps
t = 0:dt:T; %The time interated over
lt = length(t); %the number of timesteps
%%
```

A.2. MAIN CODE

```
[MU,MW,KU_inv,KW_inv]=matrix_form(par,N,dx,dt); %All the necessary matrices
%Are pre-defined in this step to avoid unnecessary expense later on

U = nan(N,lt); %matrix columns are time stamps. Fill with Nan
W = nan(N,lt);
rng(1) %now this is important. This sets the Random seed!! So it can be repeatable

U(:,1) = u1+0.02*u1*rand(length(X),1); %Setting the Initial conditions
W(:,1) = w1;

for i=1:lt-1 %Integrating over time with the Crank Nicolson method
    100*i/lt %Loading counter
    %This is the integrating step! filling the matrix within the loop
    [U(:,i+1),W(:,i+1)]=Crank_fun_revised(par,KU_inv,KW_inv,MU,MW,dt,U(:,i),W(:,i));
end

%% THIS SECTION WILL ASSIGN SINUSOIDAL INITIAL CONDITIONS BASED ON THE
%% PREVIOUSLY CALCULATED ALLOWABLE WAVENUMBERS

[MU,MW,KU_inv,KW_inv]=matrix_form(par,N,dx,dt); %All the necessary matrices
%Are pre-defined in this step to avoid unnecessary expense later on

U = nan(N,lt); %matrix columns are time stamps. Fill with Nan
W = nan(N,lt);
rng(1) %now this is important. This sets the Random seed!! So it can be repeatable
k_v = [2:10];
pert_matrix = zeros(length(k_v),length(X));
for i=1:length(k_v)
    beta = round(100*rand)
    pert_matrix(i,:) = cos(k_v(i)*(X+beta)*2*pi/100);
end

S = sum(pert_matrix,1);
S./length(k_v);

U(:,1) = u1+0.02*u1*S; %Setting the Initial conditions
W(:,1) = w1;

for i=1:lt-1 %Integrating over time with the Crank Nicolson method
    100*i/lt %Loading counter
    %This is the integrating step! filling the matrix within the loop
    [U(:,i+1),W(:,i+1)]=Crank_fun_revised(par,KU_inv,KW_inv,MU,MW,dt,U(:,i),W(:,i));
end

%% To view the simulation live over time
figure()
for i=1:100:lt-1
plot(X,U(:,i)); ylim([0 15]); grid on
drawnow

end
```


Bibliography

- Callaway, R (1995). “Positive interactions among plants”. In: *The Botanical Review* 61, pp. 306–349.
- Crank, J and P Nicolson (1996). “A practical method for numerical evaluation of solutions of partial differential equations of the heat-conduction type”. In: *Advances in Computational Mathematics* 6, pp. 207–226.
- Duffy, D (July 2004). “A critique of the Crank-Nicolson scheme, strengths and weakness for financial instrument pricing”. In: *Wilmott* 2004, pp. 68–76. DOI: 10.1002/wilm.42820040417.
- Greig, P (1979). “Pattern in vegetation”. In: *Journal of Ecology* 67, pp. 755–779.
- hilmeijer and willygovaarts (2021). MATCONT. <https://sourceforge.net/projects/matcont/>.
- Holling, C (1973). “Resilience and Stability of Ecological Systems”. In: *Annual Review of Ecology and Systematics* 4, pp. 1–23.
- J.A Sherratt, G.J Lord (2007). “Nonlinear dynamics and pattern bifurcations in a model for vegetation stripes in semi-arid environments”. In: *Theor. Popul. Biol.* 71.
- (2013). “Pattern solutions of the Klausmeier model for banded vegetation in semiarid environments V: The transition from patterns to desert”. In: *SIAM Journal on Applied Mathematics*.
- Kharab, A and R Guenther (2002). *An introduction to numerical methods : a MATLAB approach*. Chapman & Hall.
- Klausmeier, C.A (1999). “Regular and Irregular Patterns in Semiarid Vegetation”. In: *Science New Series* 284.
- Koppel, J van de, M Rietkerk, and FJ Weissing (1997). “Catastrophic vegetation shifts and soil degradation in terrestrial grazing systems”. In: *Trends in ecology & evolution* 12, pp. 352–356.
- Lefever, R and O Lejeune (1997). “On the origin of tiger bush”. In: *Bulletin of Mathematical Biology* 59, pp. 263–294.
- Lejeune, O, P Couderon, and René Lefever (1999). “Short range co-operativity competing with long range inhibition explains vegetation patterns”. In: *Acta Oecologica* 20, pp. 171–183.
- MacFayden, W (1950). “Soil and vegetation in British Somaliland”. In: *Nature* 165.
- Maini, P et al. (2012). “Turing’s model for biological pattern formation and the robustness problem”. In: *Interface focus* 2 (4), pp. 487–496.
- Maini, P.K. and M.R. Myerscough (1997). “Boundary-driven instability”. In: *Applied Mathematics Letters* 10, pp. 1–4.
- MATLAB (2022). *version 9.12.0.1927505*. The MathWorks Inc.
- Mauchamp, A., S. Rambal, and J. Lepart (1994). “Simulating the dynamics of a vegetation mosaic: a spatialized functional model”. In: *Ecological Modelling* 71, pp. 107–130.
- May, R (1977). “Thresholds and breakpoints in ecosystems with a multiplicity of stable states”. In: *Nature* 269.5628, pp. 471–477.
- Murray, JD (2003). *Mathematical Biology II: Spatial Models and Biomedical Application*. Springer.
- Owkes, M (2015). Heun’s Method Example. <https://www.youtube.com/watch?v=7BcT7kurcIY>.
- Rietkerk, M, R Bastiaansen, S Banerjee, J van de Koppel, et al. (2021). “Evasion of tipping in complex systems through spatial pattern formation”. In: *Science*. 374(6564).
- (2021). “Evasion of tipping in complex systems through spatial pattern formation”. In: *Science* 374.
- Rietkerk, M, M Boerlijst, et al. (2002). “Self-Organization of Vegetation in Arid Ecosystems”. In: *The American Naturalist* 160, pp. 524–530.
- Rietkerk, M, S Dekker, et al. (2004). “Self-Organized Patchiness and Catastrophic Shifts in Ecosystems”. In: *Science (New York, N.Y.)* 305, pp. 1926–9. DOI: 10.1126/science.1101867.
- Scheffer, M et al. (2001a). “Catastrophic shifts in ecosystems”. In: *Nature* 413, pp. 591–596.

BIBLIOGRAPHY

- Scheffer, M et al. (2001b). “*Catastrophic shifts in ecosystems*”. In: *Nature* 413, pp. 591–596.
- Schlesinger, W et al. (1996). “On the Spatial Pattern of Soil Nutrients in Desert Ecosystems”. In: *Ecology* 77, pp. 364–374.
- Shuguang, LI (2008). “*Boundary conditions for unit cells from periodic microstructures and their implications*”. In: *Composites Science and Technology*.
- Stelt, S van der et al. (2013). “*Rise and Fall of Periodic Patterns for a Generalized Klausmeier–Gray–Scott Model*”. In: *Journal of Nonlinear Science* 23, pp. 39–95.
- Thiery, J. M., J.-M. D’Herbes, and C. Valentin (1995). “A Model Simulating the Genesis of Banded Vegetation Patterns in Niger”. In: *Journal of Ecology* 83, pp. 497–507.
- Turing, A (1952). “*The chemical basis of Morphogenesis*”. In: *Philosophical Transactions of the Royal Society of London*. 237, pp. 37–72.
- Valentin, C, J.M d’Herbes, and J Poesen (1999). “Soil and water components of banded vegetation patterns”. In: *CATENA* 37, pp. 1–24.
- Weisstein, E (2022). Fourier Series. URL: <https://mathworld.wolfram.com/FourierSeries.html>.
- Wendt, J and J Anderson (2008). *Computational fluid dynamics : an introduction*. Springer.
- White, LP (1970). “Brousse Tigree Patterns in Southern Niger”. In: *Journal of Ecology* 58.2, pp. 549–553.
- Worral, G (July 2006). “The Butana grass patterns”. In: *Journal of Soil Science* 10, pp. 34–53.